Theses and Dissertations | 1. Thesis and Dissertation Collection, all items

2000-03

A computational and experimental investigation of flapping-wing propulsion

Lund, Timothy Craig

Monterey, California. Naval Postgraduate School

http://hdl.handle.net/10945/9366

NAVAL POSTGRADUATE SCHOOL
Monterey, California

THESIS

A COMPUTATIONAL AND EXPERIMENTAL
INVESTIGATION OF FLAPPING-WING PROPULSION

by

Timothy Craig Lund

March 2000

Thesis Advisor: Kevin D. Jones
Co-Advisor: Max F. Platzer

Approved for public release; distribution is unlimited.

DTIC QUALITY INSPECTED 4

20000619 024

REPORT DOCUMENTATION PAGE

Public reporting burden for this collection of information is estimated to average 1 hour per response, including the time for reviewing instruction, searching existing data sources, gathering and maintaining the data needed, and completing and reviewing the collection of information. Send comments regarding this burden estimate or any other aspect of this collection of information, including suggestions for reducing this burden, to Washington headquarters Services, Directorate for Information Operations and Reports, 1215 Jefferson Davis Highway, Suite 1204, Arlington, VA 22202-4302, and to the Office of Management and Budget, Paperwork Reduction Project (0704-0188) Washington DC 20503.

1. AGENCY USE ONLY *(Leave blank)*	2. REPORT DATE March 2000	3. REPORT TYPE AND DATES COVERED Master's Thesis

4. TITLE AND SUBTITLE A Computational And Experimental Investigation Of Flapping-Wing Propulsion	5. FUNDING NUMBERS
6. AUTHOR(S) Timothy Craig Lund	

7. PERFORMING ORGANIZATION NAME(S) AND ADDRESS(ES) Naval Postgraduate School Monterey, CA 93943-5000	8. PERFORMING ORGANIZATION REPORT NUMBER

9. SPONSORING / MONITORING AGENCY NAME(S) AND ADDRESS(ES)	10. SPONSORING/MONITORING AGENCY REPORT NUMBER

11. SUPPLEMENTARY NOTES
The views expressed in this thesis are those of the author and do not reflect the official policy or position of the Department of Defense or the U.S. Government.

12a. DISTRIBUTION / AVAILABILITY STATEMENT Approved for public release; distribution is unlimited.	12b. DISTRIBUTION CODE

13. ABSTRACT *(Maximum 200 words)*

Flapping-wing propulsion is studied experimentally and numerically. The objective of the research is to provide further insight into the aerodynamics of flapping-wing air vehicles. Experimental work is conducted in the NPS 1.5 m x 1.5 m (5 ft x 5 ft) in-draft wind tunnel. A previously constructed long-span flapping-wing model suspended by cables is used to approximate the two-dimensional nature of the numerical simulation. For this experiment, the model is configured with two wings executing plunge-only motion. Thrust is indirectly determined by using a laser rangefinder to measure streamwise displacement of the model. Results are compared with previous experimental tests. A numerical analysis is conducted using USPOT, a locally developed unsteady panel code that models two independently moving airfoils with three degrees of freedom and non-linear deforming wakes. Thrust and efficiencies are computed for harmonically oscillating airfoils. Direct comparison is made between experimental and numerical thrust measurements.

14. SUBJECT TERMS Flapping-Wing, Low Reynolds Number, USPOT, panel code, Laser Doppler Velocimetry, LDV	15. NUMBER OF PAGES 80
	16. PRICE CODE

17. SECURITY CLASSIFICATION OF REPORT Unclassified	18. SECURITY CLASSIFICATION OF THIS PAGE Unclassified	19. SECURITY CLASSIFICATION OF ABSTRACT Unclassified	20. LIMITATION OF ABSTRACT UL

NSN 7540-01-280-5500

Approved for public release; distribution is unlimited

A COMPUTATIONAL AND EXPERIMENTAL INVESTIGATION OF FLAPPING-WING PROPULSION

Timothy Craig Lund
Lieutenant, United States Navy
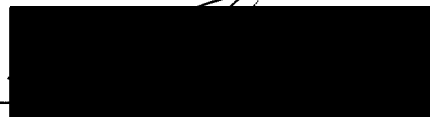B.S., University of Arizona, 1990

Submitted in partial fulfillment of the
requirements for the degree of

MASTER OF SCIENCE IN AERONAUTICAL ENGINEERING

from the

NAVAL POSTGRADUATE SCHOOL
March 2000

Author: _____
Timothy Craig Lund

Approved by: _____
Kevin D. Jones, Thesis Advisor

_____
Max F. Platzer, Co-Advisor

_____
Max F. Platzer, Chairman
Department of Aeronautics and Astronautics

ABSTRACT

Flapping-wing propulsion is studied experimentally and numerically. The objective of the research is to provide further insight into the aerodynamics of flapping-wing air vehicles. Experimental work is conducted in the NPS 1.5 m x 1.5 m (5 ft x 5 ft) in-draft wind tunnel. A previously constructed long-span flapping-wing model suspended by cables is used to approximate the two-dimensional nature of the numerical simulation. For this experiment, the model is configured with two wings executing plunge-only motion. Thrust is indirectly determined by using a laser rangefinder to measure streamwise displacement of the model. Results are compared with previous experimental tests. A numerical analysis is conducted using USPOT, a locally developed unsteady panel code that models two independently moving airfoils with three degrees of freedom and non-linear deforming wakes. Thrust and efficiencies are computed for harmonically oscillating airfoils. Direct comparison is made between experimental and numerical thrust measurements.

TABLE OF CONTENTS

LIST OF SYMBOLS

AR	aspect ratio, b^2/S
b	effective wing span
b^*	total wing span
c	chord length
C_d	drag coefficient per unit span, $D/(q_\infty c)$
C_D	drag coefficient, $D/(q_\infty S) = C_d b$
C_p	power coefficient, power/$(q_\infty S V_\infty) = -C_l \dot{y} - C_m \dot{\alpha}$
C_t	thrust coefficient, $T/(q_\infty S)$
D	drag
f	oscillation frequency in Hz
h_x	horizontal plunge amplitude in terms of c
h_y	vertical plunge amplitude in terms of c
k	reduced frequency, $2\pi f c/V_\infty$
q_∞	free-stream dynamic pressure, $\frac{1}{2}\rho_\infty V_\infty^2$
S	wing area, bc
t	time
T	thrust
V_∞	free-stream velocity
x_p	pivot location from leading edge in terms of c
$x(\tau)$	horizontal displacement in terms of c
$y(\tau)$	vertical displacement in terms of c
y	plunge displacement, in terms of c
α	angle of attack (AOA)
α_{eff}	effective angle of attack
α_{geom}	geometric angle of attack
α_{ind}	induced angle of attack
$\Delta\alpha$	sinusoidal pitch amplitude
ϕ_x	phase difference between pitch and horizontal plunge
ϕ_y	phase difference between pitch and vertical plunge
η_t	propulsive efficiency, C_t/C_p
λ	taper ratio, c_t/c_0
Λ	sweep angle
ρ_∞	free-stream air density
τ	non-dimensional time, tV_∞/c
ω	circular frequency, $2\pi f$

ACKNOWLEDGEMENT

I.   INTRODUCTION

A.   OVERVIEW

In this paper, flapping-wing propulsion is investigated experimentally and numerically. Interest in the field of flapping-wing air vehicles has been spurred by the funding of Micro-Air Vehicle (MAV) development. Potential vehicle configurations to fulfill the MAV requirement include conventional fixed-wing, flying-wing, rotary-wing and flapping-wing designs. Although MAV development has prompted this research, the vehicle under consideration is several times larger than MAV specifications. The objective of this research is to provide further insight into the aerodynamics of flapping-wing air vehicles. The ultimate goal is to provide the practical aerodynamic foundation necessary for a flapping-wing MAV. This research is limited to the aerodynamics of a flapping bi-wing air vehicle, primarily with respect to thrust production. Powerplant, structural, and stability and control issues are not considered.

Experimental work is conducted in the NPS 1.5 m x 1.5 m in-draft wind tunnel. A previously constructed long-span flapping-wing model suspended by cables is used to approximate the two-dimensional nature of the numerical simulations. A photo of the mechanism in the wind tunnel test section is found in Figure 1. For this experiment, the model is configured with two wings executing plunge-only motion. Thrust is indirectly determined by using a laser rangefinder to measure streamwise displacement of the model. Results are compared with previous experimental work.

A numerical analysis is conducted using USPOT, a locally developed unsteady panel code that models two independently moving airfoils with three degrees of freedom and nonlinear deforming wakes. Thrust and efficiencies are computed for harmonically oscillating airfoils. Direct comparison is made between experimental and numerical thrust measurements.

1
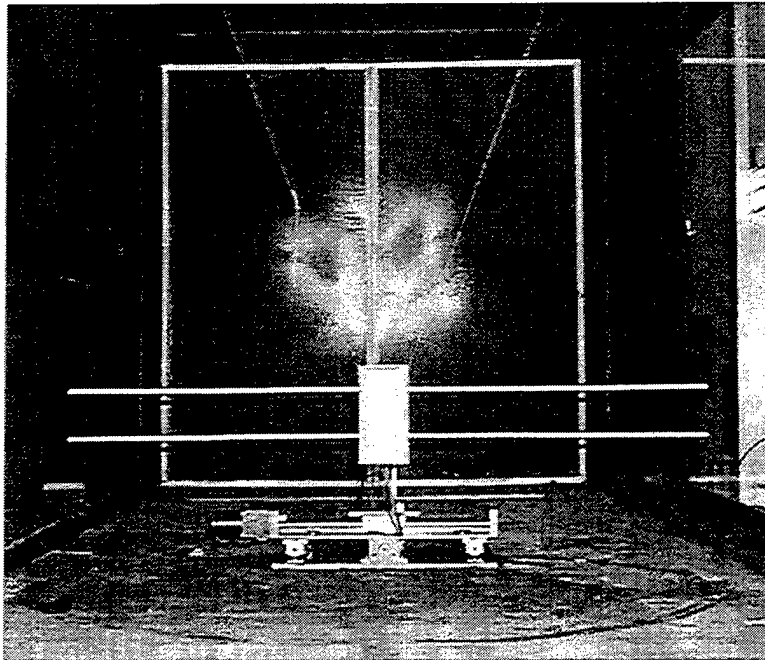
Figure 1. Flapping-Wing Mechanism in Wind Tunnel.

B. BACKGROUND

In 1992, the Rand Corporation first proposed to the Pentagon the use of Micro-air vehicles (MAVs) for aerial observation. The Defense Advanced Research Projects Agency (DARPA) became the lead agency for developing this capability. In this role, DARPA has defined MAV specifications and funded development. The aircraft are defined to be less than 15 cm square and should weigh no more than 0.113 kg. The MAV must be capable of "performing a useful military mission" and flying for 20 to 60 minutes at a clip of 9 to 18 m/s, "at an affordable cost." The technology necessary for the practical application of these vehicles is rapidly coalescing.

Due to the small size and low speed of the MAV requirement, low Reynolds number flight is encountered. Reynolds numbers less than 100,000 are typical. In the current study, the model experiences Reynolds numbers from 0 to 42,600. Since no past or current aircraft operate at these Reynolds numbers, simple geometric scaling of larger designs is not applicable to a MAV design.

DARPA requirements do not specify aircraft configuration. Potential candidates have taken the form of conventional fixed-wing, flying-wing, rotary-wing and flapping-wing designs. Low Reynolds Number flight opens a new field of investigation for all potential configurations. The current research is aimed at evaluating the aerodynamics of a flapping-wing design. Nature demonstrates that flapping wings are efficient at the Reynolds numbers of concern, and makes investigation worthwhile.

C.   FLAPPING-WING PROPULSION

Observations of nature demonstrate the effectiveness of flapping wings in creating lift and thrust. The understanding of the aerodynamics of bird and insect flight is limited, and achieving nature's effectiveness in a mechanical device has proven elusive. While all potential configurations face hurdles, the flapping-wing configuration faces the additional burden of having no previous successes as a practical flying vehicle at any scale. Some reasons for the lack of practical success in early aeronautical work with flapping wings include a lack of understanding of aerodynamic principles, as well as a lack of necessary technologies to implement the ideas. Another primary reason for the lack of success at these larger scales is the mechanical limitations of scale, where the dynamic forces of large, heavy structures make them unable to support themselves. The pursuit of this configuration is prudent in light of the small scale and relatively low dynamic forces, the examples given by nature, and previous theoretical work in the field that have shown potential efficiencies greater than other configurations.

An explanation for flapping-wing force production was first observed by Knoller [Ref 1] and Betz [Ref 2] in independent studies in 1909 and 1912, respectively. A flapping-wing creates an effective angle of attack, α_e, as depicted in Figure 2. The resulting normal force vector, N, has both lift and thrust components, L and T, respectively. Katzmayr [Ref 3] was the first to demonstrate this experimentally, in 1922. Refs. 4 - 6 provide a more detailed history of flapping wing development.
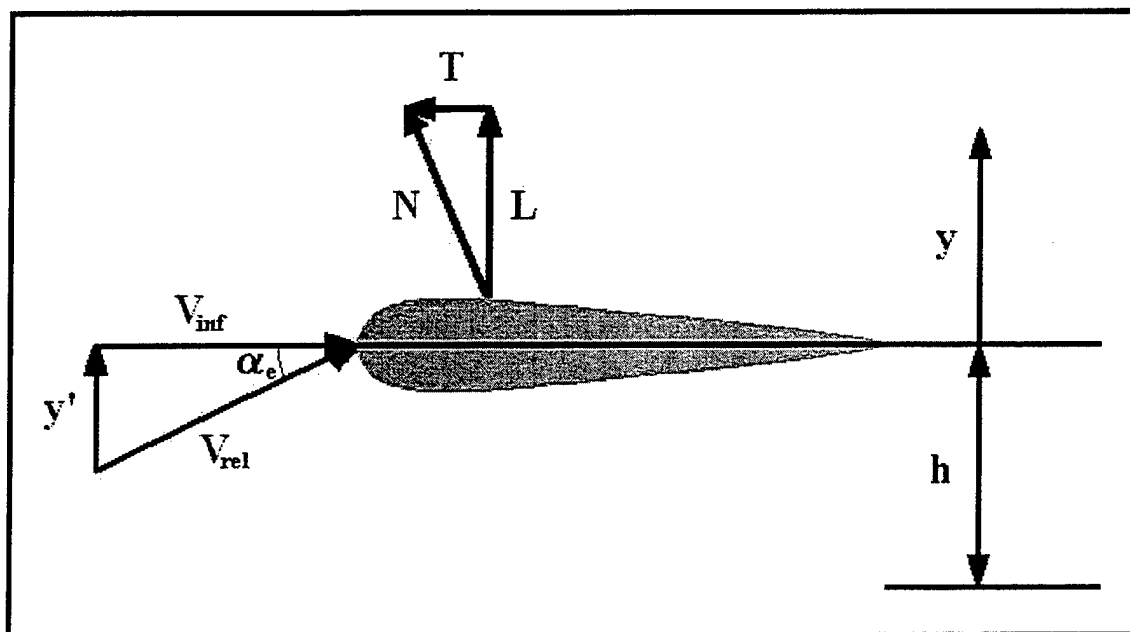
Figure 2. Effective Angle of Attack Produced by Flapping-Wing.

An infinite variety of flapping-wing configurations and dynamics are available for analysis. The parameter space is wide, including fixed and flapping airfoils, adjustment to the number and relative position of airfoils, different airfoil types, variation of pitch and plunge amplitudes and phase angles, changing pivot location and frequency, amongst others. The original intent was to explore this vast space with the numerical code and apply promising configurations to the experimental model. Delays caused by experimental equipment failures, however, subdued this ambitious project. The work has therefore concentrated on the evaluation of a single plunge-only configuration.

The most promising arrangement yielded by previous numerical and experimental work by Jones and Platzer [Ref. 4] is the two-airfoil, opposed-plunge configuration. This configuration is shown in Figure 3. The lower airfoil is equivalent to the image airfoil in ground-effect analysis. This opposed-plunge configuration holds promise in reproducing ground-effect behavior when clear of a ground plane. The beneficial effects of ground effect are seen put to use by birds, particularly over water.

When operating near the ground, downwash velocities are decreased. The ground presents a boundary condition requiring the normal component of velocity to go

4

to zero. This condition alters the streamline pattern around the airfoil. Analytic ground-effect analysis places a mirror image about the plane of symmetry. The image vortex system is opposite the original system. In order to satisfy the boundary condition, the vertical velocities induced by these two image vortex systems will cancel at the plane of symmetry. Figure 3 is a graphical representation of this ground-effect system from USPOT. In addition to vertical velocity going to zero, the destructive interference of the counter-rotating vortex systems diminishes the influence of the trailing vortices on the airfoil. The reduced influence, in turn, lessens the induced angle of attack, increasing lift and thrust. The configuration under study appropriates the beneficial aspects of ground-effect when flying out of ground-effect. In addition, the anti-symmetric motion balances the vertical force loading of any potential mechanism. [Ref 7]
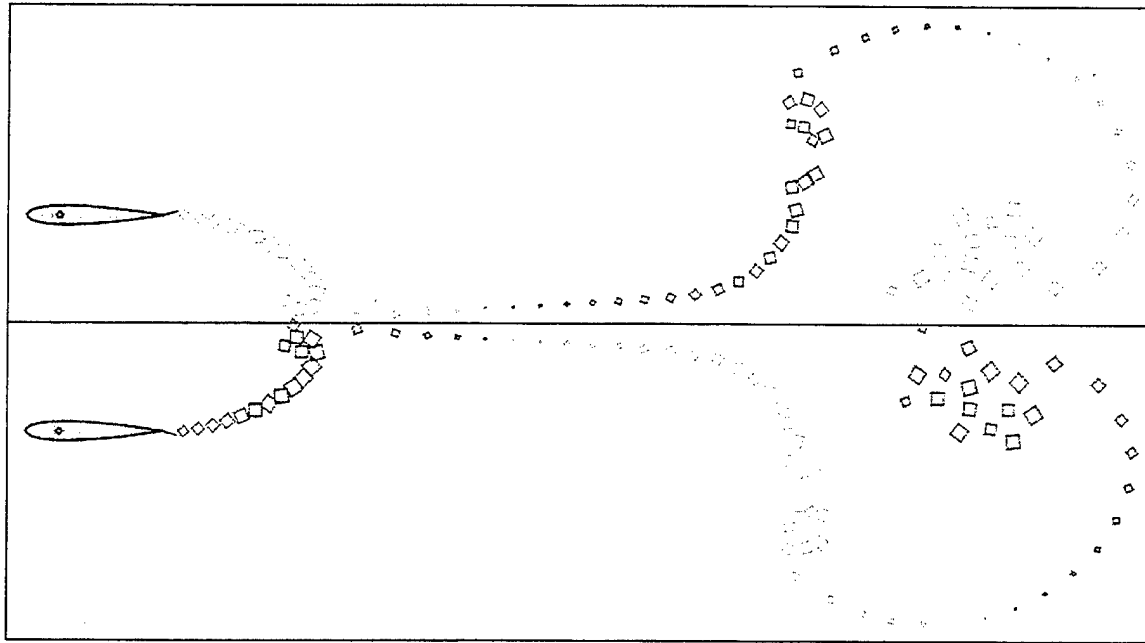
Figure 3. Airfoil in Ground Effect

In order to mimic the 2-dimensional nature of the numerical code as closely as possible, a previously constructed long-span flapping-wing mechanism was used in the experiments. The mechanism was constructed to support previous research work into this field. In addition to providing a promising configuration, the current work provided the opportunity to demonstrate repeatability with previous experiments. Repeatability is

desired as a means to validate the experimental methods, and to demonstrate that the performance of the vehicle will be consistent, something certainly required for a flying vehicle.

II. NUMERICAL ANALYSIS

A. PANEL CODE

Numerical analysis was conducted using the locally developed Unsteady Potential flow (USPOT) code. This panel code computes the incompressible flow solution to two arbitrarily placed airfoils independently executing three-degree-of-freedom motion. The original single-airfoil code (UPOT) was developed by Teng [Ref. 8] and the expanded two-airfoil code by Pang [Ref. 9]. The steady portion of the code stems from the work of Hess and Smith [Ref. 10], who originally developed the code to analyze steady, inviscid flow over an airfoil. The unsteady portion employs the method of Basu and Hancock [Ref.11].

In order to obtain the steady solution for the velocity field around the airfoil, the velocity potential, Φ, is introduced. The velocity potential is a scalar function in which velocity is given by the gradient of Φ:

$$V = \nabla\Phi \qquad \left(u = \frac{\delta\Phi}{\delta x}, v = \frac{\delta\Phi}{\delta y} \right) \tag{1}$$

The velocity potential is defined for irrotational flows only, where:

$$\nabla \times V = 0 \tag{2}$$

Flow field velocities are obtained from the velocity potential by differentiating Φ in the same direction as the velocity. The airfoil is created by combining several elementary potential flows, namely uniform, source, and vortex flow.

Introducing the definition of the velocity potential to the incompressible continuity equation,

$$\nabla \bullet V = 0 \tag{3}$$

yields the Laplace Equation:

$$\nabla^2\Phi = 0 \qquad \left(\Phi_{xx} + \Phi_{yy} = 0 \right) \tag{4}$$

Equation 4 is another statement of mass conservation. Note that this equation is a linear partial differential equation. As such, elementary flows that are irrotational and

7

incompressible can be combined to form a complicated flow pattern of the same nature (irrotational and incompressible). Linearity allows us to superimpose these solutions.

Superposition of these flows allows the creation of an airfoil of arbitrary shape. The code accomplishes this by first dividing the surface of an airfoil into n panels with dimensions that are small compared to the airfoil. A source distribution and a vorticity distribution are uniformly placed over each panel. The source strength per unit length, q_j, is constant over a panel, but may vary in strength from panel to panel. This gives n unknowns. A single vortex is evenly distributed amongst the panels to provide circulation. This vortex strength at each panel, γ, is constant. This adds another unknown ($n+1$ unknowns). Boundary conditions are necessary to solve the differential equation. Flow tangency is imposed upon the flow, requiring the flow to be tangent to the airfoil surface at the center of each panel. This provides n equations. The second boundary condition is the Kutta trailing edge condition. The condition is imposed either by requiring equal upper and lower surface pressure at the trailing edge, or by requiring the tangential velocity on both surfaces to be zero at the trailing edge. This provides one equation. There are now $n+1$ equations and $n+1$ unknowns. The computer can solve this system of linearly independent equations simultaneously for the velocity potential. [Ref. 5]

In order to account for the unsteady nature of the flow and the associated change in circulation, a wake model is used. In this model, the unsteady effects are accounted for by application of the theorems of Helmholtz. In the steady model previously described, a circulation is induced on the airfoil by the vortex elements. By Helmholtz, the total circulation remains constant. Any change in lift entails a change in circulation. This circulation change is offset by vorticity shed into the wake. [Ref. 12]

To ensure the total circulation remains constant in the code, a vorticity panel is extended from the trailing edge. This panel's function is to shed vorticity into the flow, counteracting the constantly changing circulation of the pitching/plunging airfoil. The wake panel introduces three additional unknowns. These unknowns include the vorticity panel's vortex strength, and the length and orientation of the panel. The strength of the

wake panel is equal in magnitude and opposite in direction to the change in circulation about the airfoil. The length of the panel varies according to the magnitude of the local resultant velocity at the midpoint and the time step. Lastly, the wake panel is orientated in the direction of the local velocity at the midpoint of the wake panel. At the end of each time step, the vorticity in the wake panel is concentrated into a point vortex, which is then released into the flow. The vortex convects downstream, continuing to influence the airfoil. [Ref. 5]

Figure 4 is a representation of the wake model. Γ is the circulation about the airfoil, Δ is the wake panel length, γ_w is the wake panel vortex strength, θ is the wake panel orientation, j and $j+1$ represent panel numbering, q_j is the source strength per unit length over the designated panel, γ is the panel vortex strength, and V_∞ is the free-stream velocity. The subscript k denotes the current time step and $k-1$ denotes the previous time step.

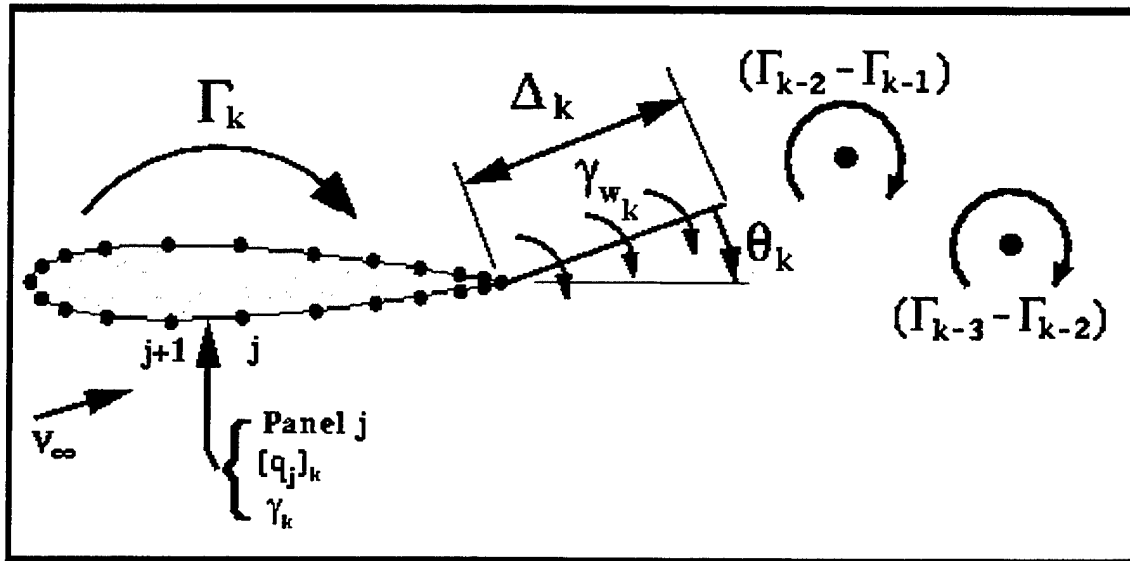
Figure 4. Schematic of the Panel Code Wake Model. From Ref. 5.

Determination of the flow tangency and Kutta condition must be solved simultaneously. An iterative procedure must be used to determine the length and orientation of the wake panel. The solutions to the potential equations are then used to solve for the velocity field about the airfoil. Application of the unsteady incompressible

9

Bernoulli equation gives the pressure distribution about the airfoil. Integrating the pressure distribution over the upper and lower surface yields forces in the direction normal to the airfoil surface. The net force is broken into components to obtain the approximation for lift and thrust. The USPOT code provides results only in a numerical output, unlike the single-airfoil code which provides a graphical representation of results.

Panel codes are subject to limitations. The Laplace equation is a simplified version of the Navier-Stokes equation applicable to incompressible flow that neglects viscous terms. The equation, therefore, does not take into account separation/stall, or the viscous boundary layer effects. This assumption of inviscid flow is most accurate with streamlined bodies. The code is only valid for incompressible flow, and is thus only useful for low-speed flows, typically flows with a Mach number less than 0.3. The code analyzes flow over a 2-D airfoil. No 3-D effects, namely wing-tip vortices, are taken into consideration. It is more accurate for predicting lift than drag, since it neglects drag induced by wing-tip vortices and skin friction drag. The code compares well with linear theory as well as other panel codes. It has been documented extensively with respect to linear theory, other numerical methods, and experimental work [Ref. 5].

B.   NUMERICAL ANALYSIS EQUATIONS OF MOTION

The generalized airfoil system of USPOT is shown in Figure 5. All lengths are scaled and nondimensionalized with respect to the first airfoil chord. Time, t, is nondimensionalized with respect to free-stream velocity, V_∞, and chord length, c:

$$\tau = \frac{tV_\infty}{c} \tag{5}$$

The airfoils are of arbitrary shape and relative position, the second being at coordinates x_2-x_1, y_2-y_1 from the first. The first airfoil chord length is one, and the second (c_2) airfoil chord length is a scale factor of the first. The pitching motions of the airfoils are independent, and are defined by an initial constant angle of attack, α_0, and the change in angle of attack, $\Delta\alpha$. Here, they are shown at angle of attack α_1 and α_2. The point about which each airfoil pivots is relative to its leading edge as a fraction of chord length (x_{p1}, x_{p2}). The frequency of the pitch is entered nondimensionally as the reduced frequency:

10

$$k = \frac{\omega c}{V_\infty} \qquad (6)$$

where ω is the circular frequency of oscillation, $\omega = 2\pi f$. The time-dependent angle of attack is given by:

$$\alpha(\tau) = \alpha_0 + \Delta\alpha\cos(k\tau) \qquad (7)$$

The code allows plunging motion in both the x and y coordinate directions. The respective plunge amplitudes, h_x and h_y, are entered as a scale factor of the first airfoil chord length. Phase angles, φ_x and φ_y, between the pitch and either plunge motion may be entered independently for each airfoil. The motion of the flapping airfoil is sinusoidal in the numerical model. The time dependent plunge position of an airfoil is given by:

$$x(\tau) = h_{0x} + h_x \cos(k\tau + \phi_x)$$
$$y(\tau) = h_{0y} + h_y \cos(k\tau + \phi_y) \qquad (8, 9)$$

where h_{0x} and h_{0y} are zero for the first airfoil.
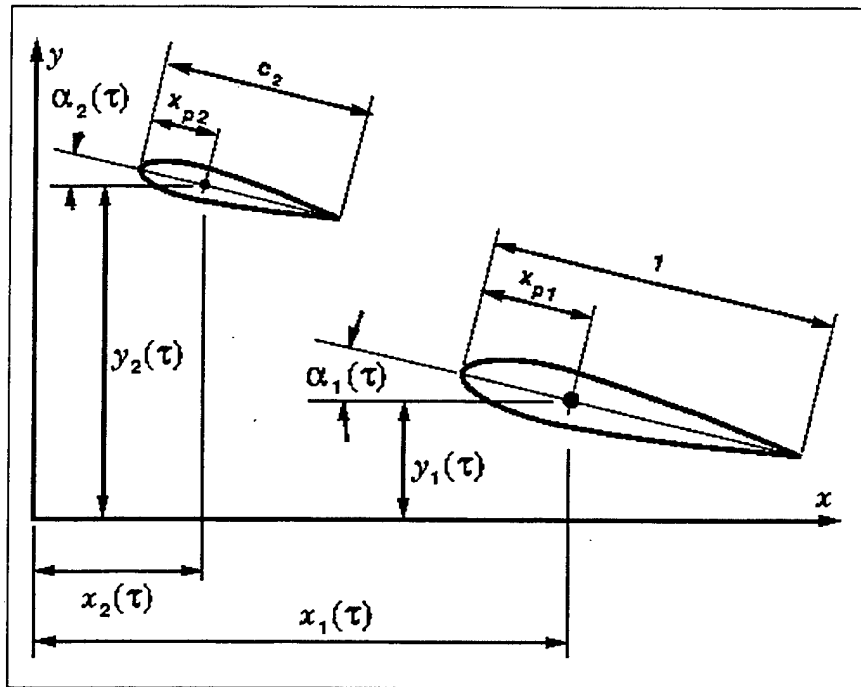
Figure 5. Panel Code Generalized Two-Airfoil System. From Ref. 5.

11

C.   LIMITATIONS OF NUMERICAL SIMULATION

As discussed in the Panel Code section, the numerical simulation is based on the Laplace equation. The code is applicable only to incompressible (low-speed) flows, and cannot predict viscous effects such as separation/stall, or the viscous boundary layer. No 3-D effects, such as cross-flow and wing-tip vortices, are accounted for.

The code is also limited to flapping at reduced frequencies ranging from approximately k=0.1 to 2.0, approximately the limits of reliable code accuracy for this configuration. The code's lower reduced frequency bound is due to singularity strength getting very small as k goes to zero. The sum of many very small numbers leads to high numerical errors. This is most prominently revealed by the propulsive efficiency, η_t. Both the thrust coefficient and power coefficient become very small with low k ($C_t \propto k^2$, $C_p \propto k^3$). Any imprecision in either coefficient will yield questionable results. Since thrust efficiency is the ratio of these two very small numbers ($\eta_t = C_t/C_p$), η_t becomes inaccurate. The code's upper reduced frequency bound is dependent upon airfoil configuration. As airfoil separation narrows and frequency increases, the code's wake model becomes unstable. The code fails to converge above approximately k=2.0 in this close proximity configuration.

D.   NUMERICAL ANALYSIS CONFIGURATION

For the work conducted, the panel code was set up to model the configuration and motion of the experimental model. The experimental model is described in the Flapping-Wing Mechanism and Experimental Configuration sections. The configuration was for an unswept, constant chord, two-airfoil system (one above the other), with plunge-only motion. The associated geometry included mean distance between airfoils, y_0=1.4c, plunge amplitude, h=0.4, and an effective angle of attack, α_e=0°. This opposing plunge configuration is depicted in Figure 6. Symmetric NACA 0014 airfoil sections were specified, flapping at reduced frequencies ranging from k=0.1 to 2.0. This limitation on reduced frequency is discussed in the previous section.
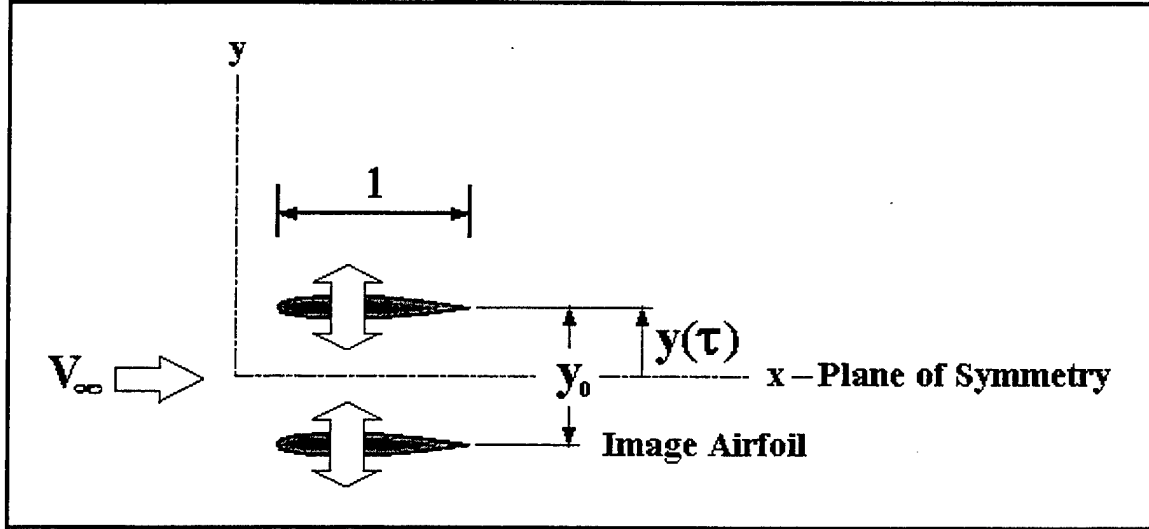
Figure 6. Airfoils in Opposed-Plunge Configuration. After Ref. 5.

The panel code's input and output are nondimensional. In order to simulate the experimental work, it was necessary to nondimensionalize the experimental data, run the panel code, then dimensionalize the data for analysis. The experimental configuration above provides the input data necessary to run the panel code, most notably the reduced frequency, k, and plunge amplitude, h_y. The panel code output consists of the lift, drag, and moment coefficients, angle of attack, and the plunge position of each airfoil. Thrust is obtained from the panel code output by dimensionalizing the drag coefficient,

$$T = -D = \frac{1}{2}\rho_\infty V_\infty^2 S C_D \qquad (10)$$

where T is thrust, D is drag, ρ_∞ is free-stream air density, S is wing area, and C_D is the drag coefficient. The wing area must be multiplied by the number of airfoils, so $S=2bc$, where 2 is the number of airfoils, b is the useful lifting span of the experimental mechanism (1200 mm), and c is the chord (64 mm). The nondimensional drag coefficient C_D is also based on the useful lifting span, so that $C_D=C_d b$.

The reduced frequency input to the panel code contains both velocity and frequency data. Expanding and rearranging the equation for reduced frequency, the following equation for velocity is obtained:

13

$$V_\infty = \frac{2\pi f c}{k} \qquad (11)$$

Dimensional velocities are obtained by entering experimental flapping frequencies (2.95, 5.01, 7.03 Hz), chord length, and reduced frequency. These procedures dimensionalized thrust, velocity, and frequency for analysis.

E.   NUMERICAL ANALYSIS RESULTS

Jones conducted an evaluation of several configurations. He compared the numerical code with Garrick's linear theory for a single flapping airfoil, and conducted a numerical analysis for the two-airfoil flapping case. The results are dimensionalized for analysis based upon the experimental flapping mechanism's geometry and dynamics described in the previous section. Figure 7 is a plot of thrust coefficient, C_t versus reduced frequency, k. The graph represents thrust per airfoil. The graph indicates good agreement between linear theory and the code for the single airfoil case. The results show that for the two-airfoil configuration, the thrust per airfoil is significantly higher than for the single airfoil case. This suggests a beneficial thrust aspect associated with the opposed-plunge motion. Since the graph represents thrust per airfoil, the two-airfoil configuration should produce well over twice the thrust of the single airfoil. As discussed in the Flapping-Wing Propulsion section, the opposed-plunge motion replicates the motion used in the analysis of airfoils in ground-effect.
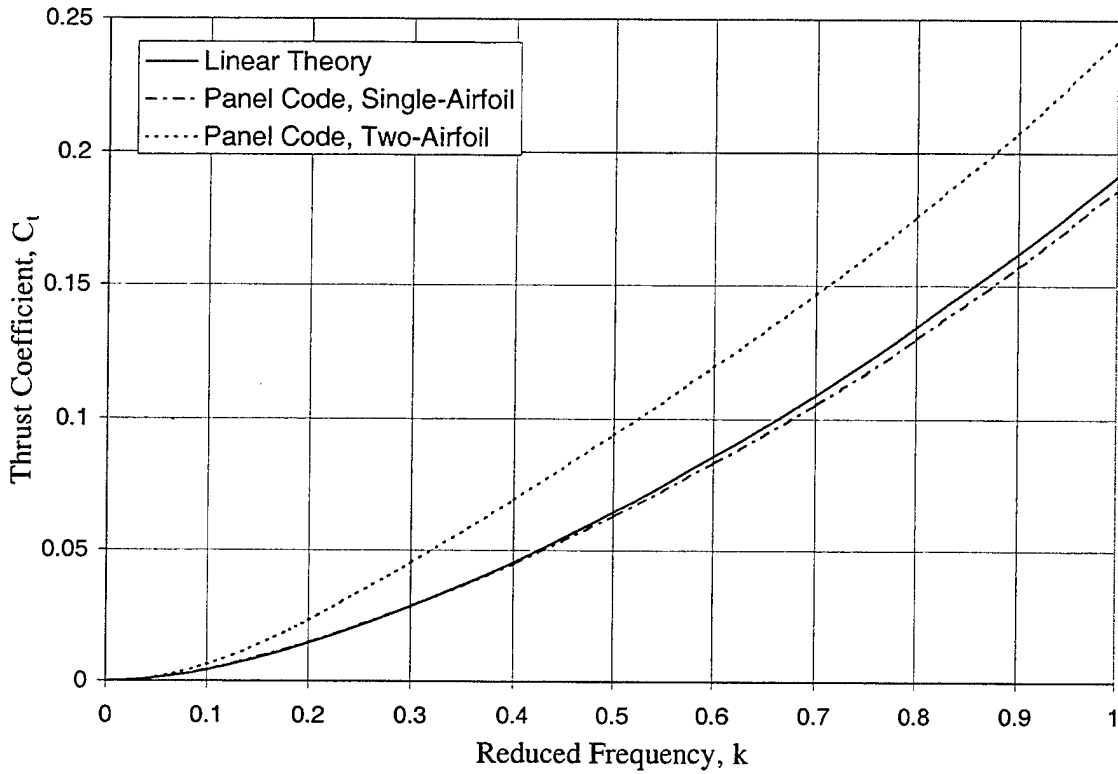
Figure 7. Thrust Coefficient per Airfoil vs Reduced Frequency. After Ref. 5.

In Figure 8, the propulsive efficiency, η_t, is plotted against k for the same configurations. The two-airfoil, opposed-plunge configuration shows higher efficiencies than the single flapping airfoil over nearly all of the reduced frequency range. The rapid drop in efficiency by the two-airfoil configuration at low k is most likely due to code limitations than actual behavior. A discussion of this limitation is contained in the Limitations of Numerical Analysis section.
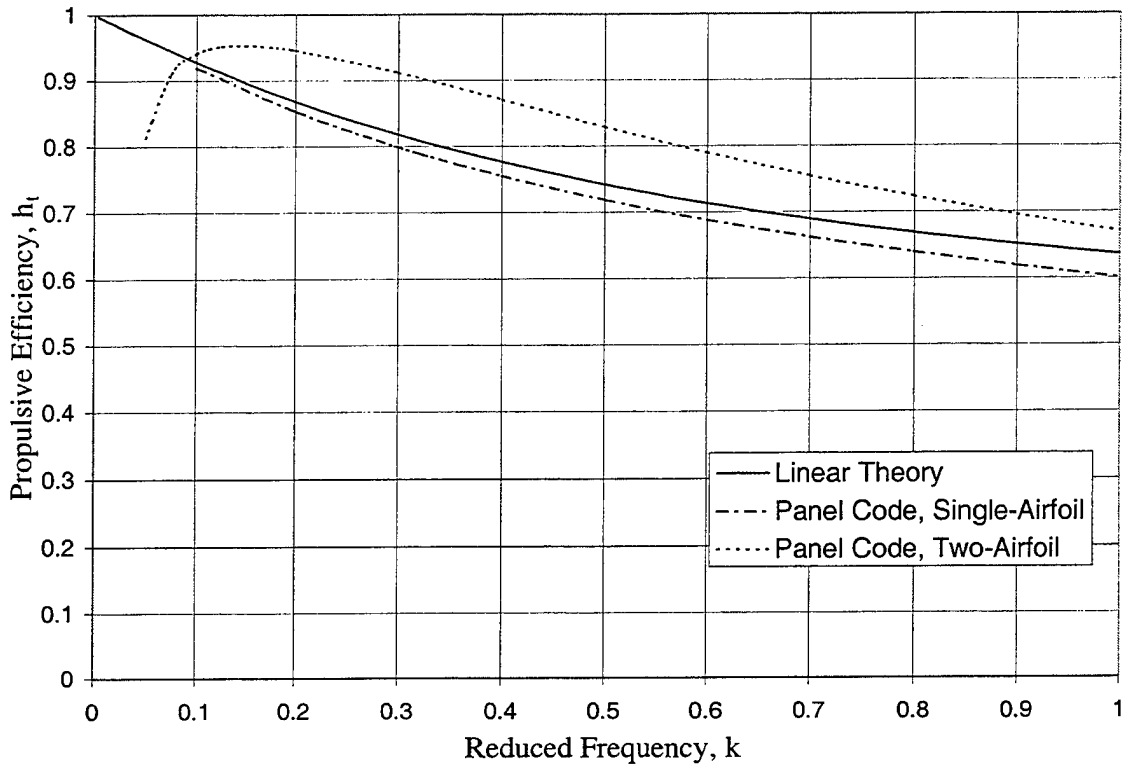
Figure 8. Propulsive Efficiency vs Reduced Frequency. After Ref 5.

The results of USPOT dimensionalized for the experimental model is presented in Figure 9. Tabular data is contained in Appendix B. Lines of constant reduced frequency and constant effective angle of attack are coincident, and are added for reference. For a single flapping airfoil, linear theory predicts thrust will increase roughly proportional to f^2. For a two-airfoil system, we see a similar behavior.
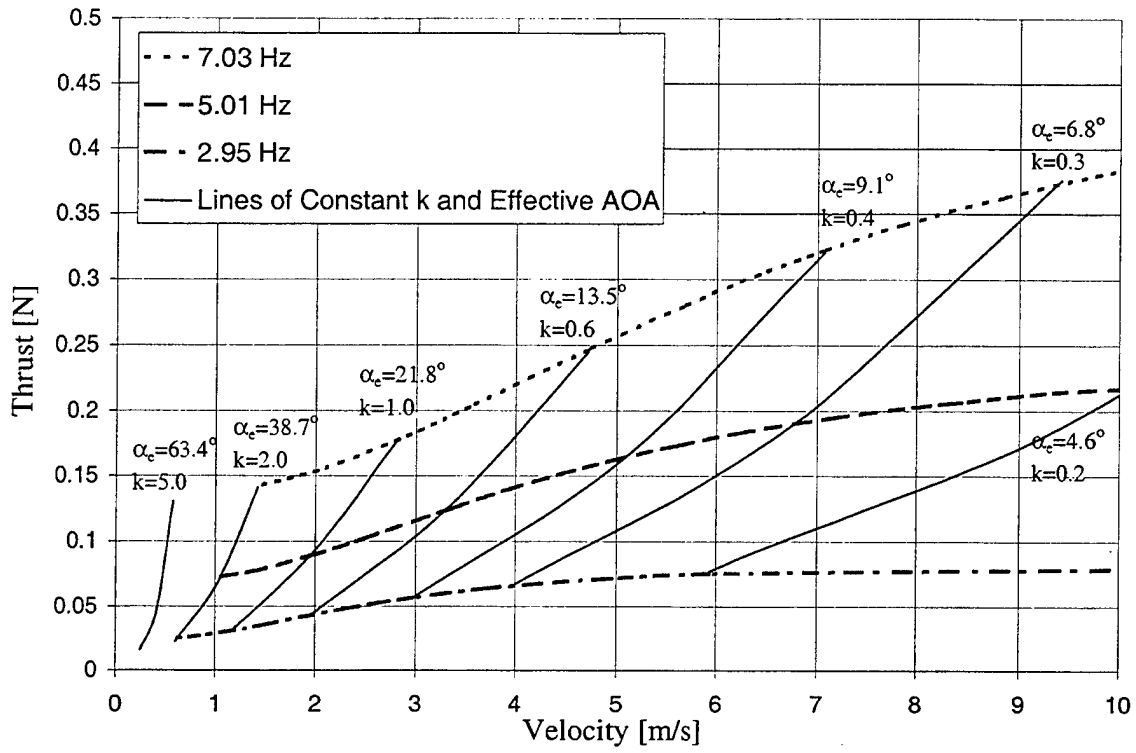
Figure 9. Thrust vs Velocity from Panel Code.

THIS PAGE INTENTIONALLY LEFT BLANK

III. EXPERIMENTAL ANALYSIS

A. EXPERIMENTAL APPARATUS

1. Flapping-Wing Mechanism

The flapping-wing mechanism used for the experiments was designed by Dr. Kevin Jones at the Naval Postgraduate School in 1997. Its construction and dynamics are described in Ref. 5, from which this description is largely taken. Isometric, profile, and top views are shown in Figure 10, Figure 11 and Figure 12. The structure of the fuselage is made of aluminum, the front and rear nacelles of balsa-wood, and the wings of wood. The device is configured to flap one or two wings. When flapping two wings, the wings are configured one above the other. The two flapping wings are configured to execute two degree of freedom motion, with both pitch and plunge amplitudes adjustable. The phase angle between pitch and plunge is also adjustable. Stationary wings may be attached before or after the flapping wings in the slots depicted.
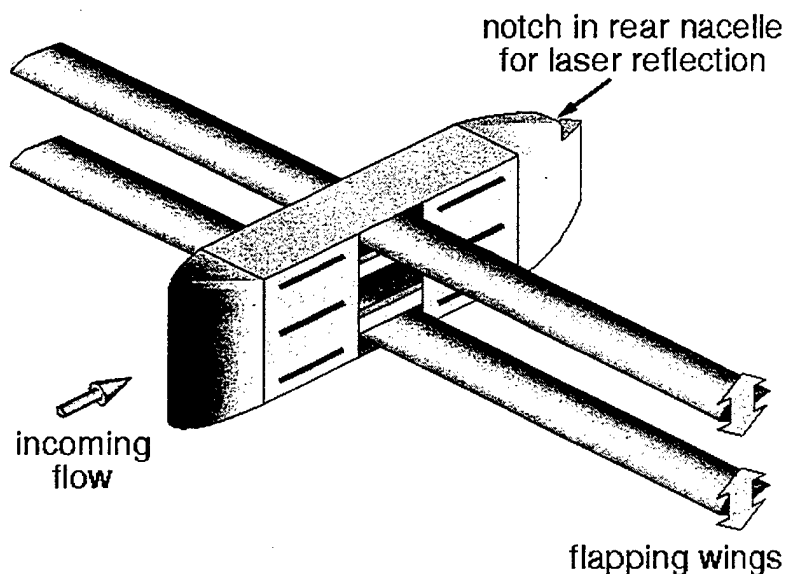
Figure 10. Isometric View of Upturned Flapping Mechanism. From Ref. 5.

actuator   bearinged   flapping   flapping   motor
wheels   pins   wings   beams
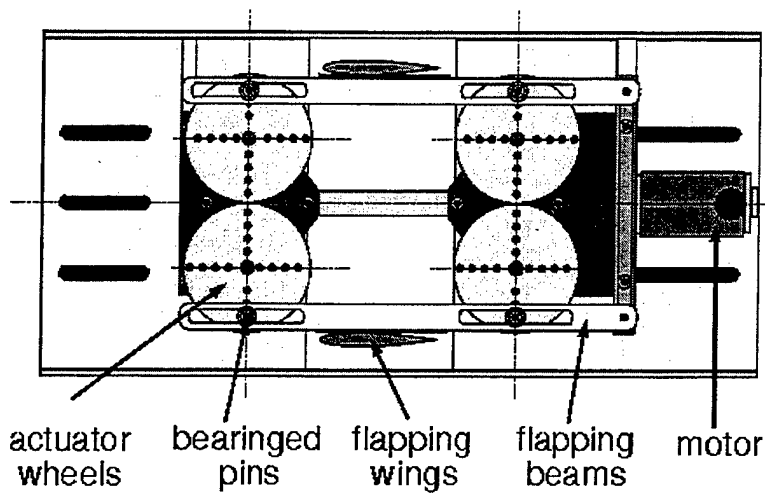
Figure 11. Profile View of Flapping Mechanism. From Ref. 5.
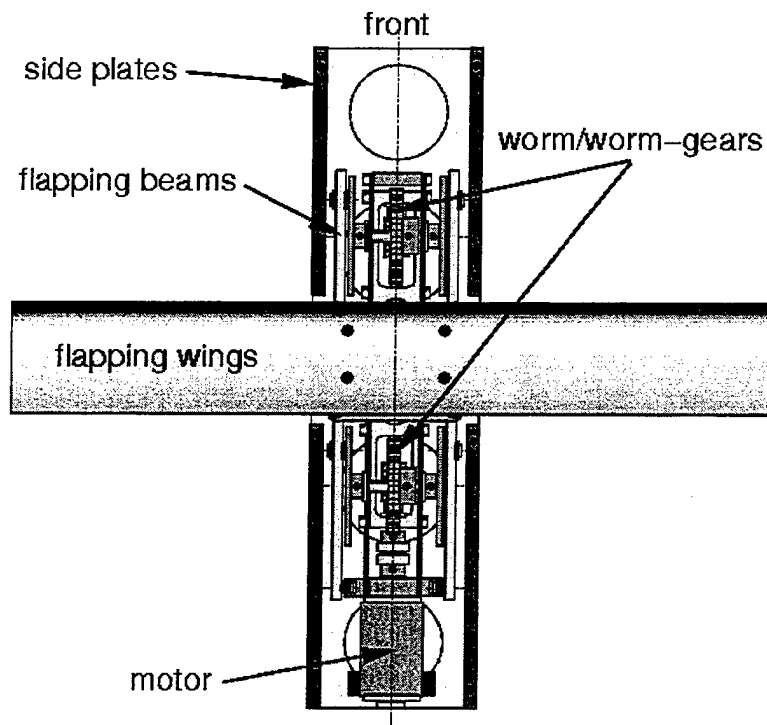
Figure 12. Top View of Flapping Mechanism. After Ref. 5.

The flapping wings are attached to moving beams, which are driven by eight actuator wheels. A pin attached to each of the eight wheels rides in a slot at the end of each beam. This attachment changes the circular motion of the wheels into the flapping motion of the beams. The beams may be attached to the wheels at a selected wheel

radius to control plunge amplitude. Wing pitch is controlled by adjusting the phase between the fore and aft wheels.

The eight wheels are attached to four worm gears. The gears mesh with two worms that are driven by an Astro-Flight Cobalt 40 model airplane motor. The motor is powered by a variable voltage/current power supply. After burning up one motor armature, the new motor's voltage was limited to 26V for a maximum of one minute. This voltage limit restricted maximum flapping frequency to 7 Hz. This corresponds to a motor rpm of 21,000 with a 50:1 gear reduction. Current draw was always less than 5A. New worms and worm gears are being ordered to obtain higher frequencies.

Two wing sections were available for the experiment. A symmetric cross-section approximating a NACA 0014 and a cambered cross-section approximating a NACA 23012. Further configuration details can be found in the Experimental Configuration section. The wings are manufactured by the Miniature Aircraft Supply model helicopter company. The wings are made of balsa wood and laminated hardwood, and covered with a thin, smooth plastic sheet. The wings can be bolted to the flapping beams, or attached as stationary wings in the slots before and after the flapping wings. The stationary wing feature is useful for experiments based upon Schmidt's wave propeller [Ref. 13]. This work suggests that a stationary airfoil in the wake of flapping airfoils may increase thrust production.

2.   Wind Tunnel

Experiments were performed in the NPS low-speed in-draft smoke tunnel depicted in Figure 13. The tunnel was modeled after the smoke tunnel of the Naval Air Engineering Lab in Philadelphia [Ref. 14]. Air is ingested from inside the building through a square 4.5 x 4.5 m inlet, converging through a 9:1 bell shaped contraction to a 1.5 x 1.5 m test section. Tunnel speed is controlled by a variable pitch fan driven by a constant speed electric motor. Motor and fan vibration are isolated from the test section by rubber sleeves on each side of the motor/fan assembly. The tunnel velocity range is 0 to 9.5 m/s.
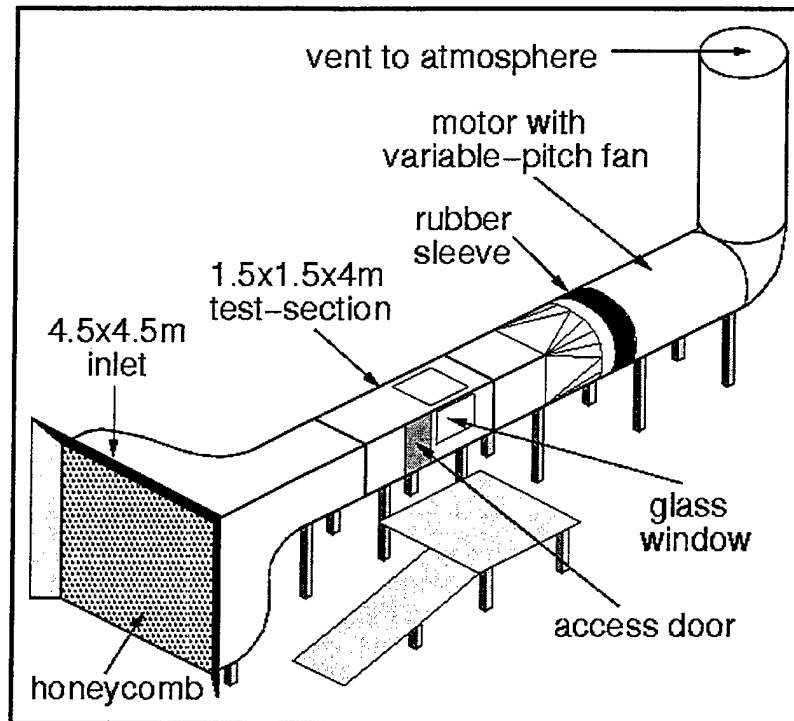
Figure 13: NPS Low-Speed In-draft Wind Tunnel. From Ref. 5.

The initial experimental effort was delayed by a tunnel fan failure. The effort required to fix the fan is described in Appendix A. A portion of the effort consisted of resetting the variable pitch fan blades to provide tunnel velocities from 0 to 9.5 m/s. This will support future very low-speed work. In addition to the fan repair, old fixtures supporting old experiments were all removed, the tunnel floor refinished, all seams smoothed and holes sealed. The old pitot-static tube and the associated fluid manometer were removed and replaced by a better positioned pitot-static tube with a higher accuracy differential pressure transducer. A tunnel calibration was performed following tunnel repairs. The test section turbulence intensity level remained below 1.75% with tunnel velocities over 1.5 m/s. Tunnel calibration is described in depth in Appendix D.

3.   Laser Doppler Velocimetry (LDV)

Laser Doppler Velocimetry (LDV) is a precise, accurate, non-intrusive method of measuring the velocity of fluid flow. LDV is an optical method that utilizes the Doppler

22

principle, measuring the frequency shift of laser light scattered by a particle in the flow. A dual-beam, on-axis, backward-scatter system was used to measure the air velocity and turbulence intensity in the NPS low-speed, open circuit smoke tunnel. A general description is provided here. Details of LDV position and sampling may be found under Experimental Data Collection, a detailed description of the LDV system and concepts in Appendix C, and LDV use for tunnel calibration in Appendix D.

In the dual-beam arrangement utilized, a beam of laser light is split in two, the frequency of one of the beams is shifted, and both beams transmitted such that they cross each other. Particles moving through the volume in space created by crossing the unshifted and shifted beams (an ellipsoid) scatter the laser light. The reflected light is collected at the probe (on-axis, backward scatter), and sent via optical receiving fiber to a Photo Multiplier Tube (PMT). A photo detector in the PMT separates the light by color, and converts it into a voltage signal at the Doppler frequency. The signal produced by the photo detector is sent to the IFA 755 signal processor via a frequency downshifter and Colorlink. The signal processor determines frequency from the electrical signal and sends these signals to the computer. The computer converts the Doppler frequency shift to velocity of the particles. Flow Information Display (FIND) software was used to display and store LDV system outputs. A detailed account of the system equipment, LDV concepts, and a system diagram can be found in Appendix C.

LDV has several advantages over other quantitative flow measurement techniques. It is a linear instrument, non-intrusive, requires no calibration, is independent of fluid density (suitable for a variety of fluids), and measures only the selected component of velocity. LDV disadvantages include high cost and sophistication, a requirement for an optical view of the flow, and the dependence on the presence of particles to scatter the light. [Ref. 15]

The initial purpose of setting up the LDV system was to determine the flow field dynamics over the flapping wings. Determination of the onset of flow separation was the primary goal. Delays caused by failures of associated and unassociated equipment, and a delay in the purchase of a longer focal length lens, prevented its use in this fashion. It is

intended that future work will use the LDV for this purpose. In the current work, the LDV was used for tunnel calibration following tunnel repairs and improvements, and also for measuring free-stream velocity at the model during testing. Tunnel calibration utilizing the LDV is discussed in Appendix D.

For experimental testing, the LDV probe was mounted on a 3-axis traverse mechanism outside the tunnel at the test section window. A photograph of the probe on its 3-axis traverse is contained in Appendix C. The LDV probe is fitted with a 350 mm lens, limiting the velocity measurements to less than a quarter of the tunnel width. A 750 mm focal length lens will be acquired soon, allowing LDV measurements to the center of the tunnel.

4.   Miscellaneous Equipment

A Rosco model 4500 smoke generator was used to provide particles for light scattering. A smoke rake was adjusted to direct smoke particles through the probe volume, ensuring the greatest scattering of laser light.

A pitot-static tube located upstream of the model was used for general adjustments to tunnel velocity. The pitot-static tube was connected to a MKS Baratron type 223B differential pressure transducer. The transducer voltage output is linear with pressure. LDV velocity measurements were used for fine tunnel speed adjustments prior to experimental runs. Data reduction was based solely on LDV velocities.

A frequency strobe light was used to get the flapping-wing frequency near that desired. The strobe was set to the desired frequency, and the wing frequency adjusted to match. The accuracy of the strobe was checked using a Monarch Instrument Tach IV Digital Optical Tachometer. Strobe error varied with frequency to a maximum of 1.5 percent in the frequencies of interest. Actual frequency used for data reduction was determined after the experiment using data from a micro-switch inside the model.

A Matsushita Electric Works Model ANL1651AC laser rangefinder was used to determine model displacement when flapping. The rangefinder was positioned behind the model at its center point distance of 13 cm. Its measurable range is 8 – 18 cm, with

accuracy decreasing with increased distance from the center point. The output of the rangefinder is 1 V/cm displacement.

A Link Instruments DSO-2102 digital storage oscilloscope was used to measure voltage. The DSO-2102 was connected to a desktop PC for display and recording of the voltage signals. The oscilloscope simultaneously records two data channels. One channel was designated for the laser rangefinder, and this data was subsequently used to determine thrust. The second channel was used to collect micro-switch data for eventual determination of flapping frequency. The oscilloscope features 32 kilobyte buffers per channel. A 1000 Hz sample rate was used, for a run time of approximately 32 seconds per thrust record.

B. EXPERIMENTAL CONFIGURATION

In the experiments conducted, the mechanism was bi-wing configured with symmetric wings approximating NACA 0014 sections. The wings were of equal chord length, separated by a mean distance of 1.4 chord lengths. The wings spanned 1270 mm; the long-span intended to replicate the two-dimensional nature of the panel code as closely as feasible. The flapping mechanism was limited to plunge-only motion. The plunge amplitude for both wings was 25.4 mm, or approximately 40 percent of the chord length ($h \cong 0.4$). The experimental configuration is shown in Table 1.

Wing Configuration		Bi-wing flapping, no stationary wings
Wing Type		Symmetric, approximating NACA 0014
Wing Span	b*	1270 mm
Fuselage Width		70 mm
Useful Lifting Span	b	1200 mm
Wing Chord	c	64 mm
Aspect Ratio	$AR=b^2/S=b/c$	19.84 full span, 18.75 useful span
Taper Ratio	$\lambda=c_t/c_o$	1
Sweep Angle	Λ	0°
Mean Wing Separation		1.4c
Plunge Amplitude	h	$h \cong 0.4 = 25.4$ mm
Pitching Motion	$\Delta\alpha$	None, $\alpha_{geom} = 0°$
Flapping Frequency		3, 5, 7 Hz (Actual 2.95, 5.01, 7.03 Hz)
Velocity	V_∞	0 - 9.5 m/s
Reduced Frequency	k	$0.12 - \infty$

Table 1. Experimental Configuration.

C. EXPERIMENTAL DATA COLLECTION

The tunnel velocity, thrust, and flapping frequency were needed in order to take useful measurements. First, the tunnel velocity was set with the pitot-static tube, then fine tuned with the LDV. The pitot tube was located 2.5 meters upstream of the model. Immediately prior to taking thrust measurements, LDV free-stream velocity sampling was conducted at the model. The LDV was positioned at the test section window at the nose of the model. The focal point was 0.35 m into the tunnel (All LDV measurements were taken with a 350 mm focal length lens positioned as close as possible to the tunnel glass), and 0.25 meters above the model. Runs were conducted every 0.5 m/s from 0 to 5 m/s, every 1.0 m/s from 5 to 9 m/s, and a final run was made at maximum tunnel speed of

9.5 m/s. Each measurement run consisted of 10,000 samples taken over a period of 3 to 10 seconds, dependent upon smoke density. This LDV free-stream velocity and associated velocity fluctuations were recorded for subsequent data reduction.

The experimental arrangement for measuring thrust is depicted in Figure 14. A photo of the model in the tunnel is shown in . The model is suspended with four thin cables 112.8 cm in length. The cables allow displacement along the streamwise axis, but hinder motion in other axes. In order to determine thrust, the model displacement due to flapping was required. Drag induced by tunnel velocity deflected the model rearward. Flapping the wings of the model propelled the model forward. The net displacement was measured by the laser rangefinder, positioned on a two-axis traverse behind the model, reflecting the beam from a notch in the model's rear nacelle.
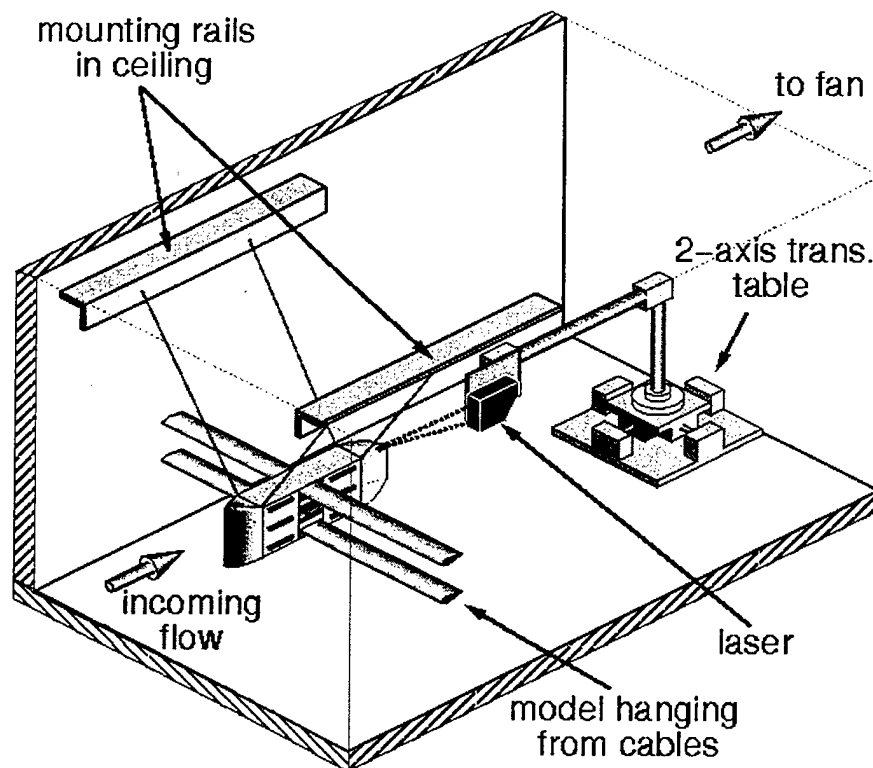
Figure 14. Flapping Mechanism in Wind Tunnel Test Section. From Ref. 5.

After setting tunnel velocity, the laser rangefinder was positioned at its zero voltage center point, 13 cm behind the model. Since the model's rearward displacement due to drag increased with velocity, the rangefinder was reset to its center point at each

27

tunnel velocity. The model's drag varied slightly dependent on wing position. The oscilloscope displayed a clear decrease in drag when the wings were closer. The model was flapped at an extremely low frequency, on the order of 0.1 Hz. This displacement, essentially representing its no-flap (0 Hz) condition, was recorded. The mean displacement of the model, therefore, took into account the variation in drag with wing position. The model was then flapped at 3, 5 and 7 Hz. Displacement voltages were again recorded. The mean displacement of the no-flap condition (its 'static' position) was subtracted from flapping displacements prior to calculating thrust at 3, 5 and 7 Hz.

In order to obtain the desired frequency, the strobe light was set to 3, 5, or 7 Hz, and the motor voltage was adjusted until the beams flapping the wings appeared to be stationary. This method was used to set frequency during experimental runs. For the ensuing data reduction, determination of flapping frequency was based on a voltage signal from a micro-switch within the model. The micro-switch was triggered once per cycle. The reduced frequencies corresponding to tunnel velocities from 0 - 9.5 m/s and flapping frequencies from 2.95 - 7.03 Hz were k=0.13 - ∞.

The flapping mechanism was not intended to be a flying vehicle, and weighs approximately 4 kg. The maximum model displacement from flapping, therefore, was a modest 1.10 cm. The laser rangefinder voltage was recorded concurrently with the frequency micro-switch voltage by the digital oscilloscope. The rangefinder and frequency micro-switch data were recorded with a sample rate of 1000 Hz for a period of approximately 32 seconds. This ensured a good census of thrust data, measuring between 94 and 225 cycles per run.

D.   EXPERIMENTAL DATA REDUCTION

After completing data collection, each of the 16 velocity-frequency combinations had an associated velocity files from the LDV and a voltage file from the oscilloscope. For each of these experimental runs, the LDV FIND software calculated the mean and standard deviation of the velocity. LDV velocity data can be found in Appendix G.

Before converting the oscilloscope voltage to force, a thrust calibration of the model was necessary. A thread attached to the model was strung over a pulley, and

known weights were hung on the thread. The model was deflected and allowed to return to an equilibrium position. The tunnel was closed to prevent air circulation from affecting the model's displacement. A 60-second voltage sample of the model's displacement was recorded by a digital voltmeter. This was conducted three times for each weight. The mean and standard deviations of the voltages from the three runs were averaged, and a calibration curve plotted. An approximately linear relationship was established between the weight and the laser rangefinder displacement voltage. The data and calibration curve can be found in Appendix E.

The voltage files from the oscilloscope consisted of voltages from both the rangefinder and frequency micro-switch. A MATLAB program, found in Appendix F, was written to convert the data into useful form. The program accomplishes this by first converting the data to voltage, then correcting for oscilloscope zero voltage offset. The thrust voltage is converted to force by means of the thrust calibration. The program identifies each cycle by the trip switch data. Figure 15 is a pictorial representation of the program's cycle counting. The voltage, thrust, and frequency are calculated for each cycle. The minimum, maximum, and average deviation of the frequency is calculated from the cycle data, as well as mean thrust. Errors associated with measuring thrust are also calculated, and are described in the Error Analysis section. Partial cycle data at the beginning and end of each thrust record is disregarded. Data is stored to two files, one containing all data for a given frequency-velocity combination, and one to a file containing a summary of all frequency-velocity combinations.
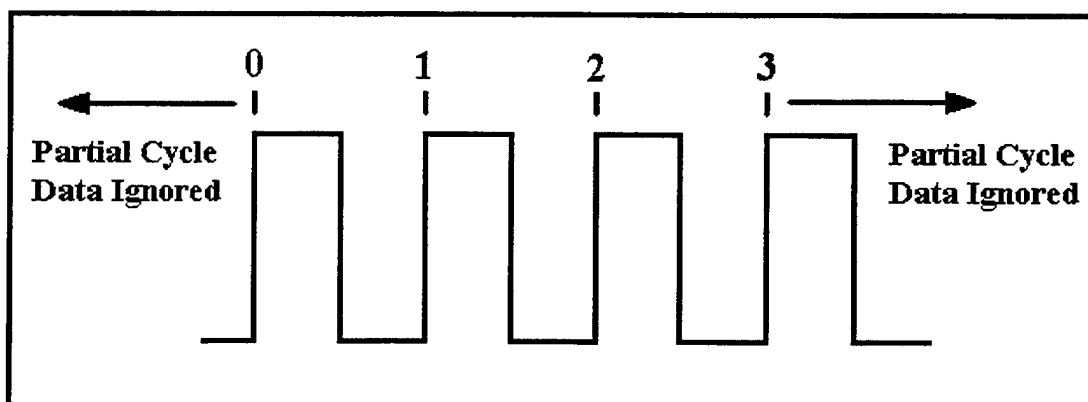
Figure 15. Pictorial Representation of Program Cycle Counting.

29

E. EXPERIMENTAL RESULTS AND ANALYSIS

1. Experimental Results

The results of the opposing plunge experiments are presented in Figure 16. Tabular data can be found in Appendix G. The trends imitate the numerical results presented in Figure 9. Frequencies are mean frequencies, all cycles varying less than 0.05 Hz from the mean, with an average frequency error of 0.9%. Error bars are added for both thrust and velocity. The sources of error are analyzed in the Error Analysis section.
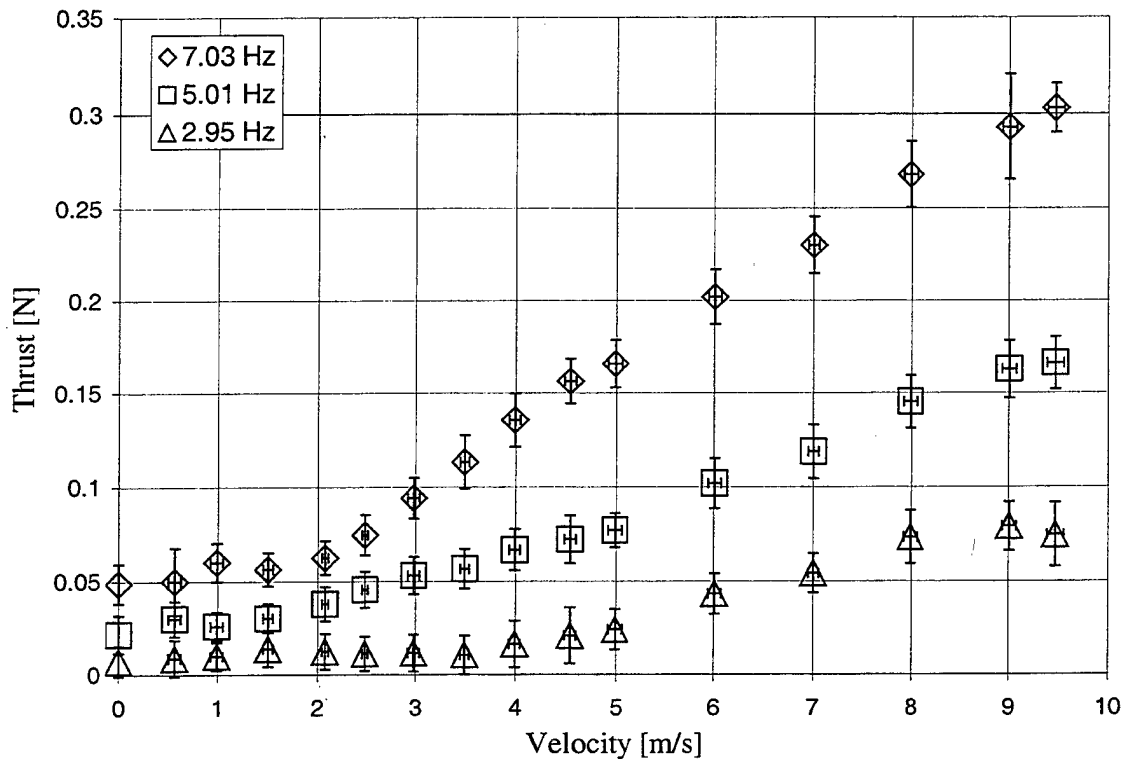
Figure 16. Experimental Thrust vs Velocity.

2. Error Analysis

There are four primary sources of error associated with the experimental thrust measurements. These four include the average deviation error, laser rangefinder error, oscilloscope error, and weight/thrust calibration error. The sum of these four errors is

presented as error bars in Figure 16. The individual and total thrust errors are presented in Appendix G. The velocity measurements taken by the LDV are very accurate. Errors associated with LDV measurements are normally very small. The velocity error bars displayed in Figure 16 represent one standard deviation added and subtracted from the mean LDV velocity. The LDV data is contained in Appendix G.

The first source of thrust error is thrust average deviation. The mean thrust for every complete flapping cycle of the model was calculated. This cycle mean thrust of the model varies from cycle to cycle. This variation is due to a variety of factors. The most significant contributor is most likely that the tunnel intake is indoors. Although the tunnel room is vented to the outside by several banks of windows, the opening and closing of doors and other windows in the building caused slight velocity drift which affects model displacement and thrust. Average deviation is similar to standard deviation in that it provides a measure of the width of the data about the mean. It is a more robust estimator, and is given by the equation below [Ref. 16].

$$ADev(x_1...x_N) = \frac{1}{N} \sum_{j=1}^{N} |x_j - \bar{x}| \qquad (12)$$

For this application, x represents the mean of each cycle, j is the cycle counter, N is the total number of cycles, and $\bar{x}$ is the mean of all cycles. The average deviation was calculated at every frequency and velocity and is considered here to be an estimated error bound. It is the predominant source of error for velocities above approximately 4 m/s.

The second source of thrust error was the laser rangefinder. Rangefinder error consists of a fixed error at the center point (13 cm). A linear error proportional to the distance from the center point is added to the fixed error at all other points. For the ranges encountered here, the rangefinder accuracy is given by the following equation:

Range Error = 0.1mm ± 0.2% * *Distance from Center Point* (13)

The thrust error associated with the rangefinder is the most significant source of error for velocities below approximately 4 m/s.

The third source of thrust error was due to the digital oscilloscope. An analysis of the 8-bit oscilloscope accuracy was conducted against a calibrated voltage source and against three voltmeters (voltmeters having higher voltage measurement accuracy). A

31

zero voltage offset in the oscilloscope was subtracted from all voltage measurements. Also, an error due to the maximum resolution of the oscilloscope was added to all voltage measurements. This error varies with the selected maximum value of the displayed vertical axis. The highest accuracy is obtained when the voltage signal approaches the maximum displayable, but does not exceed the display window. The oscilloscope accuracy analysis indicated that the actual oscilloscope error was always less than half of its resolution. Statistically, this is reasonable in that errors would tend to occur on both sides of the actual voltage, offsetting each other. In the interest of a conservative analysis, however, the maximum resolution was used as the error.

The fourth and final primary source of error was that associated with the thrust calibration. As discussed in the Experimental Data Reduction section, three 60-sec voltage runs were conducted for each weight. The mean voltages were averaged, and a near-linear calibration curve plotted. The standard deviations were also calculated. The standard deviation at a particular thrust level was applied as an error due to thrust calibration. The error was negligible and had the least impact on total error. The calibration data and curve can be found in Appendix E. The error caused by the calibration can be found in Appendix G.

3.   Comparison with Previous Experimental Work

In 1998, Jones used the same model in several configurations for experimental work. Jones conducted the experiments at 2, 4, 6, and 8 Hz, and the results of the work are presented in Ref. 5. The plunge-only experimental work is compared with the current results in Figure 17. Jones' work (even frequencies) is presented as solid characters, the current work (odd frequencies) with open characters. Jones' measurements were taken on two separate occasions and the data combined, hence the two points for each frequency in the static case.

32
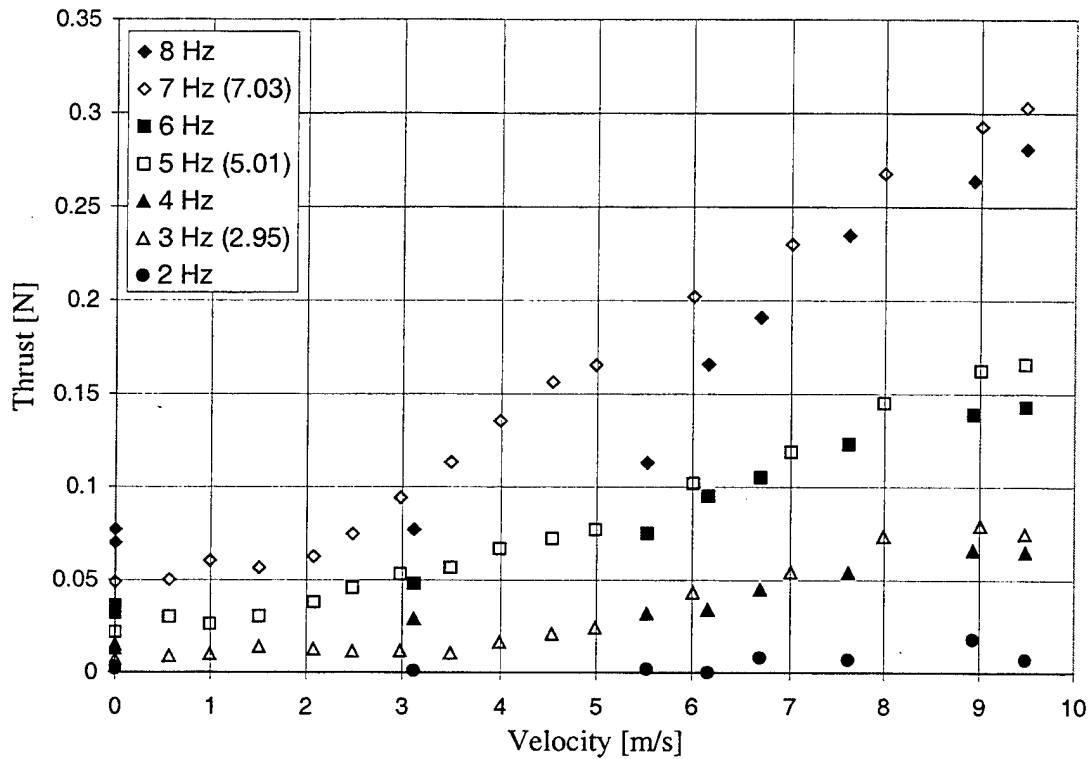
Figure 17. Thrust vs Velocity Comparison w/ Jones.

Linear theory and the numerical code imply that thrust will increase with velocity. The experimental data reflects this trend throughout the velocities tested. Linear theory and the numerical code also imply that thrust will increase as the frequency squared. Individually, the experimental data sets from both the current work and Jones confirmed this expectation. When combined, both data sets confirmed this expected trend in the static case. The combined data sets, however, did not reflect this at velocity. The current work showed higher thrust levels at 3, 5, and 7 Hz than obtained by Jones at 4, 6 and 8 Hz, respectively. One of the primary reasons for conducting the experiments was to demonstrate the repeatability of the experiment. Repeatability is necessary in order to demonstrate that the output will be consistently obtained, something certainly required for a flying vehicle. In this case, the experimental data does not initially confirm repeatability.

33

An examination of the experimental data indicates that the tunnel velocities recorded by the fluid manometer in the earlier work were inaccurate. Replicating the measurements is not possible since both the pitot tube and manometer have since been replaced. Research into work conducted after the pitot tube and manometer were replaced, but before the tunnel velocity range was changed during a fan overhaul, found only one set of experiments was conducted. This set of experiments used a newly installed LDV system, but measured at a different tunnel position. An assessment was made of the maximum velocities recorded in each experiment, and also the position of the velocity measurements and the model. This assessment indicated that the recorded velocities were roughly 30% too high. To account for this velocity error, a scaling error was applied to the manometer data, shifting the non-static, even frequency thrust data to lower velocities. This error correction is applied in Figure 18. This correction indicates that the thrust does indeed increase with frequency, as anticipated. The correction suggests that the experiment is repeatable, and that a steady thrust can be consistently produced.
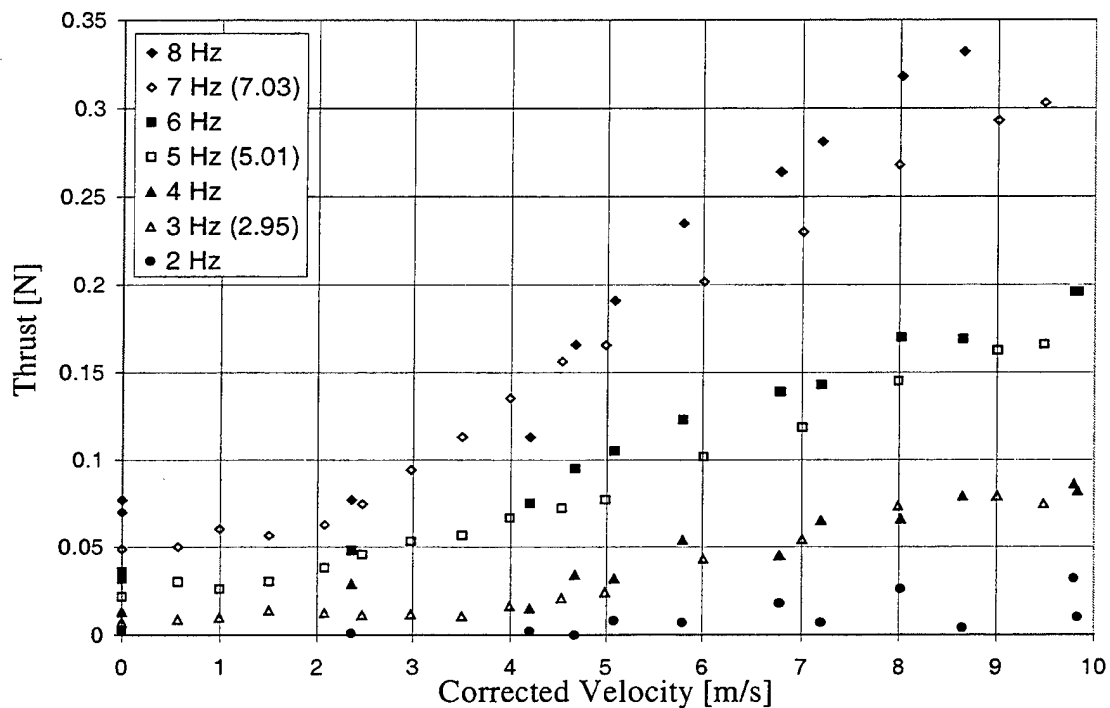
Figure 18. Thrust vs Corrected Velocity Comparison w/ Jones

34

F.   COMPARISON OF EXPERIMENTAL AND NUMERICAL RESULTS

The experimental and numerical results of the plunge-only configured flapping-wing mechanism at the frequencies analyzed are shown in Figure 19.
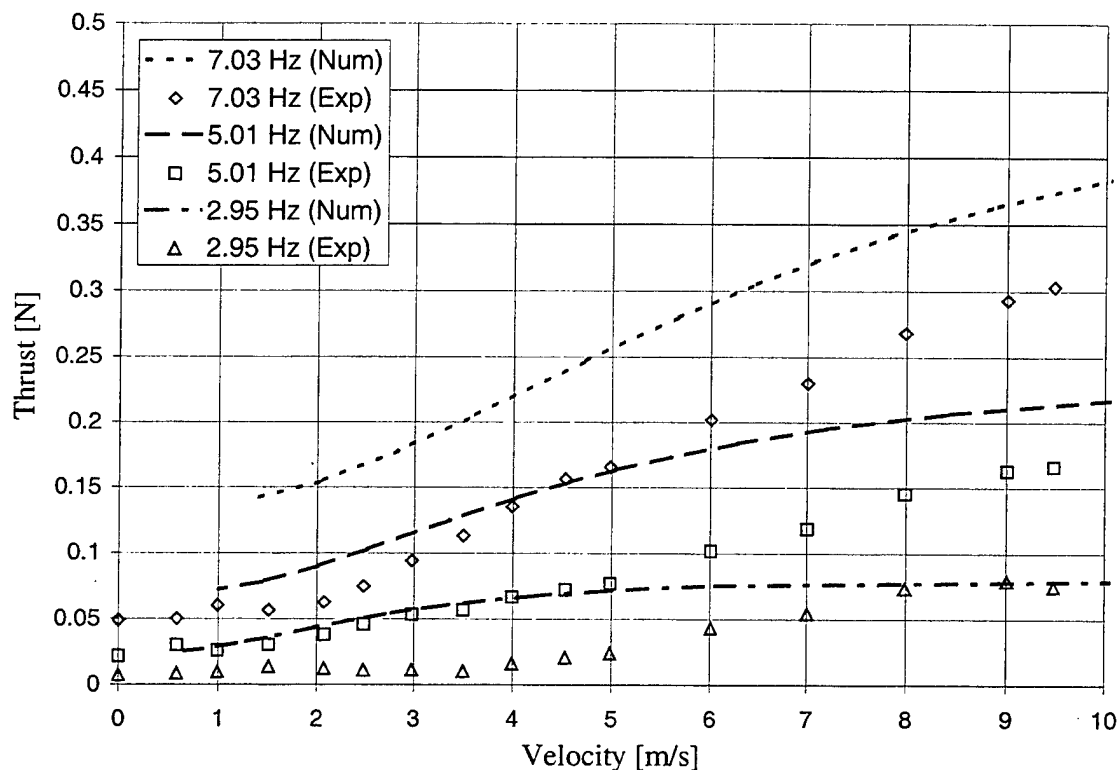
Figure 19. Thrust vs Velocity for Experimental and Numerical Data.

The numerical code is unable to predict static thrust. The numerical predictions are limited to reduced frequencies from k=0.1 to 2.0. These restrictions on k are discussed in the Limitations of Numerical Simulation section. As expected, the panel code predicts thrust consistently higher than that achieved in the experiments. The steady-state drag was subtracted from both the numerical and experimental results. The computed thrusts, therefore, eliminate the viscous boundary layer drag effects. In general, the experimental data follows the numerical data trends.

Three potential factors have been identified for the discrepancies between experimental and numerical results. The numerical model does not account for 3-D losses, namely wing-tip vortices. The numerical code also does not account for

separation. Figure 9 shows the high effective angles of attack seen by the wings at high k. While the NACA 0014 has a relatively high stall angle, 13°, the wings experience an effective angle of attack of 38.7° at k=0.1. Although separation is delayed by the plunging motion, localized separation is most likely occurring just above the static stall angle. Lastly, the model wings are subject to flexing, with the tips experiencing higher amplitudes than the roots. The amplitude varies with frequency, and there is an associated phase lag. This effect will tend to raise the experimental values artificially high, aggravating the difference between the experimental and numerical thrusts. The wings may also flex in torsion, but measurements were not attempted. In general, the difference between numerical and experimental thrust may be attributed primarily to separation, three-dimensional effects and the flex in the airfoils of the experimental model.

IV. CONCLUSIONS

Observations of nature demonstrate the effectiveness of flapping wings in creating lift and thrust. The relatively recent interest in Micro-Air Vehicle development has spurred interest in developing a flapping-wing MAV. Due to the small size and low speed of MAVs, all potential MAV configurations encounter low Reynolds number flight, a new field of study. The flapping-wing MAV has the additional burden of having no previous successes as a useful flying vehicle at any scale. The basic science and technologies necessary to employ a mechanical device in the MAV role are rapidly maturing. Nature hints that flapping wings are efficient at the Reynolds numbers of concern. The potential efficiency of this design makes investigation worthwhile.

A numerical and experimental investigation of flapping-wing propulsion was conducted. Although prompted by MAV development, the vehicle under consideration is several times larger than MAV specifications. The size was dictated in the interest of gaining an initial understanding of flapping-wing propulsion and low Reynolds number flight, verifying a numerical code, eventual smoke visualization, and general ease of assembly. The analysis was limited to the aerodynamics of flapping-wing propulsion.

The numerical analysis was conducted using USPOT, a locally developed panel code. The code models two independently moving airfoils with three degrees of freedom. Thrust and efficiencies were computed for two harmonically oscillating airfoils executing plunge-only motion. The numerical analysis established the general performance trends for opposed-plunge flapping-wing thrust. The code confirmed the expectations of linear theory, indicating thrust increases roughly as the square of the frequency.

Experimental work was conducted in the NPS 1.5 m x 1.5 m in-draft wind tunnel. A previously constructed long-span flapping-wing model suspended by cables was used to approximate the two-dimensional nature of the numerical flow. For this experiment, the model was arranged in a bi-wing configuration with the wings executing plunge-only motion. Thrust was indirectly determined by measuring the streamwise displacement of

37

the model due to flapping. The steady-state drag was subtracted from the computed thrust in order to minimize viscous boundary layer drag effects.

The experimental results were compared to Jones' previous work with the model in the same configuration. The current work was conducted at different frequencies. The data sets reflected an increase of thrust with velocity, a trend indicated by both the linear theory and the numerical code. Individually, the experimental data sets from both the current work and Jones also confirmed the expected trend of increasing thrust with increasing velocity. When combined, however, the current work showed higher thrust levels at 3, 5, and 7 Hz than obtained by Jones at 2, 4 , and 6 Hz, respectively. An examination of the previous work indicated that the recorded tunnel velocities were too high. Shifting the old data to account for this velocity error corrected this discrepancy. The corrected data reflects that thrust does increase with frequency, as anticipated. The correction suggests that the experiment is repeatable, and that a steady thrust can be consistently produced.

Direct comparison was made between experimental and numerical thrust measurements. As expected, the panel code predicts thrust consistently higher than that achieved in the experiments. The difference between numerical and experimental thrust may be attributed primarily to separation, three-dimensional effects, and wing flex in the experimental model. In general, the experimental thrust values follow the numerical value trends.

V.   RECOMMENDATIONS

The parameter space associated with flapping-wing propulsion is broad. An infinite variety of flapping-wing configurations and dynamics are available for analysis. The difficulty of evaluating this space is greatly eased by numerical methods. Programs can be easily written to continuously change and analyze potential candidates. A program for analyzing output data would contribute to the speed of analysis. The numerical analysis can play a vital role in determining promising experimental configurations.

Experimentally, efforts should be greatly eased by the tunnel fan overhaul and general clean-up, installation of new equipment for data collection, standardization of measurement techniques, and standardization of data reduction. Promising configurations can be readily tested. Experimental testing could be improved with the addition of a sting to measure lift and thrust simultaneously.

Newly acquired smoke equipment and high-speed photographic equipment should greatly aid in smoke visualization studies. Flow visualization will provide a better understanding of flow dynamics, primarily by identifying flow separation. In addition, the installation of the LDV system and LDV probe traverse mechanism should allow for mapping the complex flow field of the flapping wings.

The identification of the source of divergence between numerical and experimental results could be investigated. The difference is currently attributed to separation, three-dimensional effects, and wing flex in the experimental model. Experimentally, 3-D effects can be minimized with tip plates, either attached to a trailing stationary wing or external to the model. Wing tip flex and phase angle can be measured for application to the numerical code. A numerical strip analysis can be done by applying the model's varying spanwise wing deflection and phase angle to the code.

THIS PAGE INTENTIONALLY LEFT BLANK

APPENDIX A. EXPERIMENTAL EQUIPMENT FAILURES

The scope of this thesis has been limited by time spent repairing old equipment and installing new equipment. The initial experimental effort was delayed by a tunnel fan failure. Fan disassembly indicated worn bearings. The fan assembly was removed, cleaned, bead blasted, and the blades painted. The 32 fan bearings, one thrust and one roller bearing for each of the 16 blades, were removed and replaced. The tunnel motor was inspected and motor bearings greased. Fan shaft bearings were inspected and greased. The fan was reassembled and blades reset with uniform reduced pitch on each blade. Check runs following repairs and subsequent experimental work has demonstrated significantly reduced vibration levels. The reduction in blade pitch has changed the tunnel velocity range from 1 – 10.5 m/s to 0 – 9.5 m/s.

Initial LDV velocity measurements following tunnel repair indicated high vertical velocity at the test section. It was suspected that tunnel fan swirl was effecting upstream flow. Adjustable vanes just upstream of the fan were in a state of disrepair. The vanes were removed and honeycomb installed. In addition, general tunnel clean-up included removal of old experimental fixtures, tunnel floor refinishing, and smoothing of tunnel walls and ceiling by sealing holes and smoothing seams. The old pitot-static tube and the associated fluid manometer were removed and replaced by a better positioned pitot-static tube with a differential pressure transducer. A flood damaged 3-axis traverse mechanism was disassembled and cleaned, one motor replaced, and mounted at the test section window to support LDV measurements.

Subsequent to the installation of downstream honeycomb and tunnel clean-up, LDV velocity measurements again indicated high vertical velocities. An examination of the LDV data indicated an inconsistent output. A series of difficulties were experienced with the LDV system, culminating with loss of lasing. A technician realigned and cleaned the laser mirrors. The old LDV processing equipment was replaced by new equipment. The signal processor was replaced (IFA 755 for IFA 550), and a Colorlink Plus Receiver installed. A new DMA board and software were installed on a new computer. The new LDV system has posed no problems. A description of the LDV

system can be found in the Experimental Apparatus section and Appendix C. Tunnel turbulence intensity levels are discussed in Appendix D.

The flapping-wing mechanism's motor armature was burned up during one experimental run. The motor was removed and replaced. The new motor's voltage was limited to 26V for a maximum of one minute. This voltage limit restricted maximum flapping frequency to 7 Hz.

The smoke equipment proved difficult to use for LDV measurements. Recently acquired smoke equipment and high-speed photographic equipment should greatly aid in smoke use for LDV and visualization studies.

The accuracy of the oscilloscope used for voltage measurements came into question during experimental runs. The oscilloscope was replaced with a Link Instruments DSO-2102 digital storage oscilloscope. The oscilloscope connects to a desktop PC for display and recording of the voltage signals. The oscilloscope is described in the Miscellaneous Equipment section.

Experimental configurations can now be more readily tested. The tunnel fan overhaul and general clean-up, installation of new equipment for data collection, standardization of measurement techniques, and standardization of data reduction should greatly ease experimental efforts.
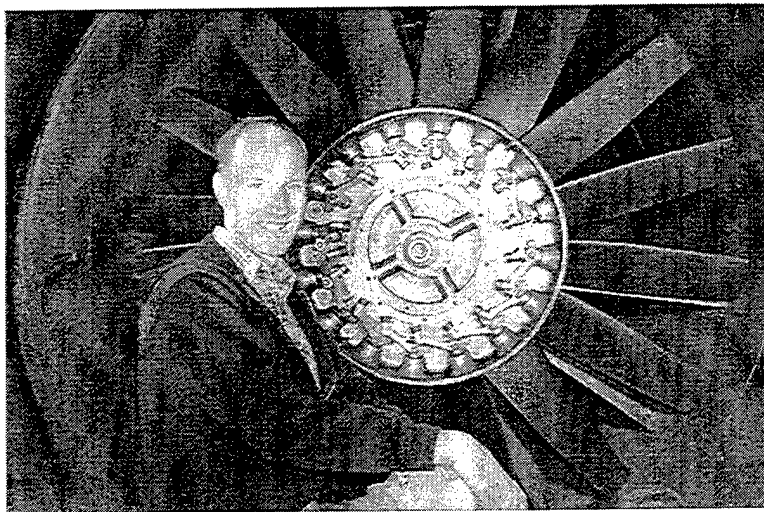
Figure 20. Tunnel Fan Complete.

42

APPENDIX B. NUMERICAL DATA

Two NACA 0014 airfoils, one atop the other, equal chordlength, $\alpha_{geom}=0$, separated by mean of 1.4c, plunge-only motion w/ plunge amplitude h/c=0.4

USPOT Data

USPOT at 2.95 Hz

Vel [m/s]	Thrust [N]	Eff η_t	Red freq k
11.859	0.08058	0.92475	0.10
5.929	0.07534	0.93556	0.20
4.941	0.07160	0.92392	0.24
4.235	0.06768	0.90946	0.28
3.706	0.06381	0.89338	0.32
3.294	0.06011	0.87642	0.36
2.965	0.05664	0.85910	0.40
2.695	0.05346	0.84177	0.44
2.372	0.04921	0.81630	0.50
1.976	0.04333	0.77646	0.60
1.482	0.03567	0.70877	0.80
1.186	0.03128	0.65492	1.00
0.847	0.02709	0.57124	1.40
0.593	0.02503	0.47743	2.00

USPOT at 5.01 Hz

Vel [m/s]	Thrust [N]	Eff η_t	Red freq k
20.138	0.23238	0.92475	0.10
10.069	0.21727	0.93556	0.20
8.391	0.20648	0.92392	0.24
7.192	0.19520	0.90946	0.28
6.293	0.18403	0.89338	0.32
5.594	0.17334	0.87642	0.36
5.035	0.16335	0.85910	0.40
4.577	0.15416	0.84177	0.44
4.028	0.14193	0.81630	0.50
3.356	0.12497	0.77646	0.60
2.517	0.10287	0.70877	0.80
2.014	0.09019	0.65492	1.00
1.438	0.07811	0.57124	1.40
1.007	0.07217	0.47743	2.00

USPOT at 7.03 Hz

Vel [m/s]	Thrust [N]	Eff η_t	Red freq k
28.273	0.45804	0.92475	0.10
14.137	0.42827	0.93556	0.20
11.781	0.40699	0.92392	0.24
10.098	0.38475	0.90946	0.28
8.835	0.36273	0.89338	0.32
7.854	0.34167	0.87642	0.36
7.068	0.32198	0.85910	0.40
6.426	0.30387	0.84177	0.44
5.655	0.27975	0.81630	0.50
4.712	0.24633	0.77646	0.60
3.534	0.20276	0.70877	0.80
2.827	0.17778	0.65492	1.00
2.020	0.15396	0.57124	1.40
1.414	0.14226	0.47743	2.00

43

THIS PAGE INTENTIONALLY LEFT BLANK

APPENDIX C. LASER DOPPLER VELOCIMETRY (LDV)

A.   INTRODUCTION

Laser Doppler Velocimetry (LDV), also referred to as Laser Velocimetry (LV), was utilized for measuring flow velocity and fluctuations. Although sophisticated and expensive, it provides a non-intrusive, very accurate means of measuring fluid particle velocity. Its dependence on optical access and particles of proper size in the flow to measure velocity can introduce complications. A general description is provided under Experimental Apparatus, the details of LDV position and sampling under Experimental Data Collection, and LDV use for tunnel calibration under a separate Appendix. This section is intended to provide more details of the system used and the concepts associated with LDV.

B.   LDV APPARATUS

The LDV system is depicted in Figure 22. The system uses a 5W, water-cooled Coherent Innova Series Argon-ion laser for the light source. A TSI Model 9201 Colorburst multicolor beam separator unit is used to separate the laser colors (green - *514.5nm*, blue - *488nm*, and purple - *476nm*), split the beams and frequency shift one beam in each color. After splitting the beams, one of the two blue beams and one of the two green beams was frequency shifted 40 MHz. The purple channel was blocked. The beams were coupled into a 2-component, 4-beam, Model 9832 fiber-optic probe through a Model 9271 coupler (one for each beam). The beams were transmitted to the probe via optical receiving fiber. Probe beam spacing was 50 mm and the lens focal length was 350 mm. The photo of the probe at the test section window is shown in Figure 23. A multi-mode receiving fiber located in the probe received and forwarded the reflected light to a Model 9160 photo multiplier tube (PMT). Although the probe is a two-component unit, only one component of the receiving optics was available. Thus, only single component measurements were possible at a given time. The output of the PMT was connected to a 9186A frequency downshifter. The downshifter is connected to a TSI

45

Model IFA-755 signal processor via the Colorlink Plus Multicolor Receiver. The Colorlink Plus contains an integral PMT and frequency downshifter. The probe connector in use, however, is incompatible with the Colorlink Plus. As such, an older stand-alone PMT and downshifter were used. In this setup, the Colorlink Plus serves no purpose except to relay the signal from the downshifter to the IFA-755 signal processor. The signal processor distinguishes the signal burst from the noise based upon the signal-to-noise ratio. The processor determines frequency, phase, burst transit time, and burst arrival time and sends these signals to the computer. The DMA board and FIND for Windows software package on the computer converts the signals into velocity, and is used for data display and storage.

LDV requires no calibration, but does require a simple alignment. The probe was aimed at a black wall. Each of the three colors in the Color Burst Module have adjustments for changing the beam's X, Y and Z position as well as tilt. Adjustments were made to the blue and the green laser spots to obtain the highest intensity (brightest). These adjustments ensure that the beam entering the fiber-optic cable is within the Brewster angle limitations. Significant signal losses occur if the beam does not enter the fiber-optic cable at the proper angle.

C.   LDV PROCESSING CONCEPTS

1.   Interference fringe spacing.

Interference fringes are formed when two light waves interfere at a crossing point. Interference fringes are a set of bright and dark bands across the probe volume, formed in the plane of the beams. The component of velocity measured is perpendicular to the bisector of the angle formed by the beams, i.e. perpendicular to the fringes. The fringe spacing value is required for velocity calculations. The FIND software determines fringe spacing automatically with either the focal length and beam spacing, or the half angle, κ. A pictorial representation of the LDV beam geometry is found in Figure 21 and a summary of the calculations involved follows.
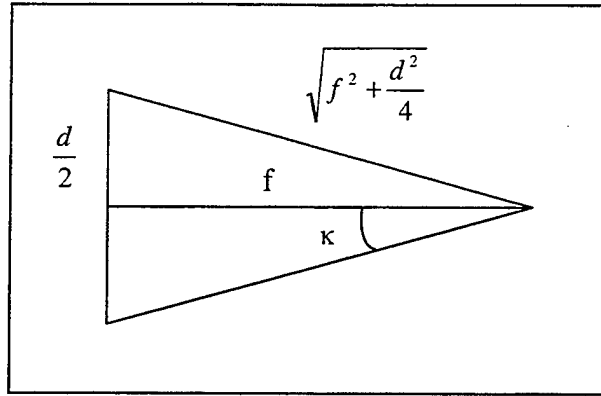
Figure 21. LDV Beam Geometry.

Fringe spacing, d_f, is related to the wavelength of the incident light, λ, and the half angle between the two beams, κ, by:

$$d_f = \frac{\lambda}{2 \sin \kappa} \tag{14}$$

The frequency detected at photodetector, f_D, can be related to the free-stream velocity in the x-direction, V_x by the following:

$$f_D = \frac{V_x}{d_f} \tag{15}$$

Trigonometry establishes the relationship between the beam spacing, d, and the focal length, f.

$$\sin \kappa = \frac{d}{\sqrt{4f^2 + d^2}} \; ; \cos \kappa = \frac{2f}{\sqrt{4f^2 + d^2}} \tag{16, 17}$$

For the probe used, the beam spacing is fixed at 50 mm, and a lens with a focal length of 350 mm was used exclusively.

Combining Equations 14 and 16 gives:

$$d_f = \frac{\lambda \sqrt{4f^2 + d^2}}{2d} \tag{18}$$

This Equation demonstrates that fringe spacing is constant for a given LDV configuration. Calculating the fringe spacing from the known values of the wavelength

47

of green light, focal length, and beam spacing yields a fringe spacing of 3.6107 μm. The half angle equals 4.086°. [Ref. 15]

2. Signal Processor

The IFA 755 signal processor has a low-pass and a high-pass filter to limit data collection to Doppler frequencies of interest. The tunnel velocity range is approximately 0 to 10 m/s. Applying Equation 15, the expected Doppler shift frequency, f_D, was calculated. The low and high-pass filter settings for the velocities of interest are contained in Table 2.

LDV Low and Hi-Pass Filter Frequency Range				Velocity Range			
				Green		Blue	
				d_f=3.6107 mm		d_f=3.4247 mm	
Low	Low [Hz]	Hi	Hi [Hz]	Low [m/s]	Hi [m/s]	Low [m/s]	Hi [m/s]
30 kHz	30000	300 kHz	300000	0.108	1.083	0.103	1.027
100 kHz	100000	1 MHz	1000000	0.361	3.611	0.342	3.425
300 kHz	300000	3 MHz	3000000	1.083	10.832	1.027	10.274

Table 2. LDV Doppler Frequency Filter Settings.

The colorburst multicolor beam separator unit was used to split the blue and green beams and frequency shift one beam of each color. The split beams were frequency shifted 40 MHz. The frequency downshifter shifted this frequency 39.8 MHz, for an effective frequency shift of 0.2 MHz (200 kHz). As the frequency goes down, the system resolution goes up. Downshifting, therefore, improves resolution to allow more precise measurement of the flow velocity. A zero velocity flow then would have a frequency of 200 kHz measured at the photo detector (i.e. no Doppler shift). Positive flows should have frequencies above 200 kHz and negative flows less than 200 kHz.

3. Probe Volume Characteristics

The properties of the probe volume are calculated by the following equations:

$$d_{e^{-2}} = \frac{4\lambda f}{\pi D_{e^{-2}}}, \quad d_m = \frac{d_{e^{-2}}}{\cos \kappa}, \quad l_m = \frac{d_{e^{-2}}}{\sin \kappa} \qquad (19, 20, 21)$$

48

$$Vol = \frac{\pi d_{e^{-2}}^3}{6\cos\kappa\sin\kappa}, \quad N_{FR} = \frac{d_m}{d_f} = \frac{1.27d}{D_{e^{-2}}} \qquad (22, 23)$$

where d_e is the diameter of the intersecting region of the probe volume, D_e is the diameter of the beam at the focusing lens (D_e=1.0 mm), d_m is the probe volume diameter across the fringes, l_m is the probe volume length, Vol is the probe volume, and N_{FR} is the number of fringes. A summary of probe volume characteristics, including the application of the above equations, is listed in Table 3.

Characteristic	Value	
Color	Green	Blue
Wavelength, λ	514.5 nm	488.0 nm
Lens focal length, f	350 mm	
Beam spacing, d	50 mm	
Half angle between beams, κ	4.086°	
Fringe Spacing, d_f	3.6107 μm	3.4247 μm
Diameter of beam at focusing lens, D_e	1.0 mm	
Beam diameter , $d_{e^{-2}}$	229.28 μm	217.47 μm
Probe volume diameter, d_m	229.86 μm	218.02 μm
Probe volume length, l_m	3.218 mm	3.052 mm
Probe volume, Vol	0.0888 mm^3	0.0758 mm^3
Number of Fringes, N_{FR}	63.7	

Table 3. Summary of Probe Volume Characteristics.

4. Velocity and Turbulence Intensity

The Flow Information Display (FIND) software calculates the mean velocity of the flow by taking the mean of the samples taken at one data point. The number of samples taken per data point is selected by the user. The software calculates the velocity by multiplying the Doppler sift by the fringe spacing. That is,

$$F_D = f_s + f_D = f_s + \frac{V}{d_f}$$ (24)

whrere F_D is the Doppler frequency measured at the photo detector, f_s is the selected frequency shift (200 kHz downshift), f_D is the Doppler shift caused by flow velocity, and V is the speed of the flow (0 - 9.5 m/s). The software also determines the turbulence intensity at each data point.

5. Seeding and Data Rate

LDV is an optical method measuring the frequency shift of laser light scattered by particles passing through the probe volume. The probe volume is an ellipsoid formed by the crossing of the laser beams. LDV measures the velocity of the particles passing through the probe volume, not the fluid. If no particle passes through the volume, no velocity is measured. System accuracy is not only dependent upon the presence of particles, but also upon the particles following the flow, and on the particles scattering light well. Particles that meet these criteria are approximately 1 μm. If the particles are too small, they scatter light that is not strong enough for a good signal but are strong enough to be accepted by the processors. The result is a noisy signal. In most experiments with air, artificial seeding is required. Flow seeding is done by atomizers that produce uniform particles that disperse in the flow. A Rosco Model 4500 smoke generator was used in this experiment. The data gathered produced a statistically well-defined scatter of velocity. Improper seeding (either undersize particles or overseeding) would have resulted in noise.
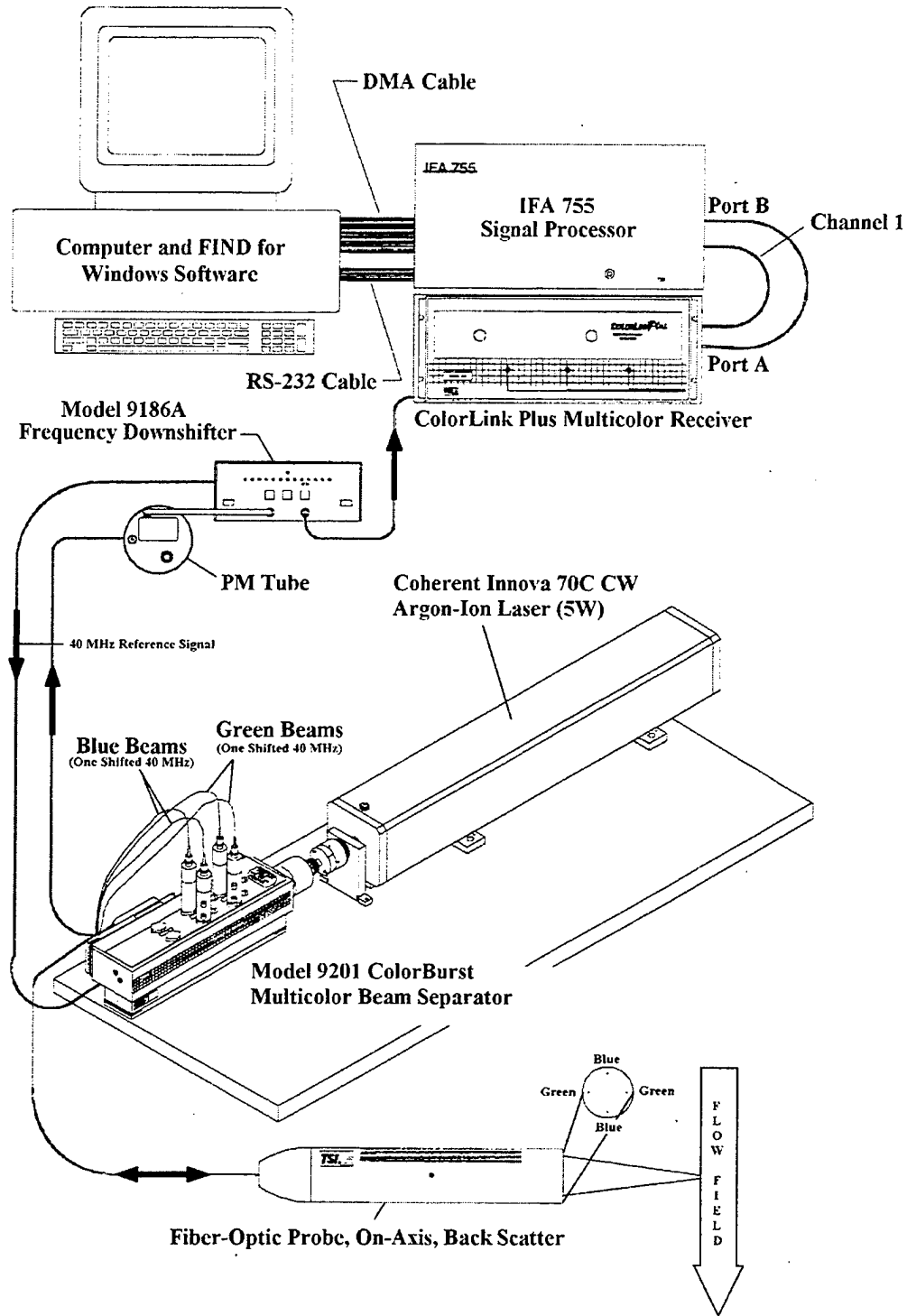
Figure 22. LDV Setup. After Ref.s 17 and 18.
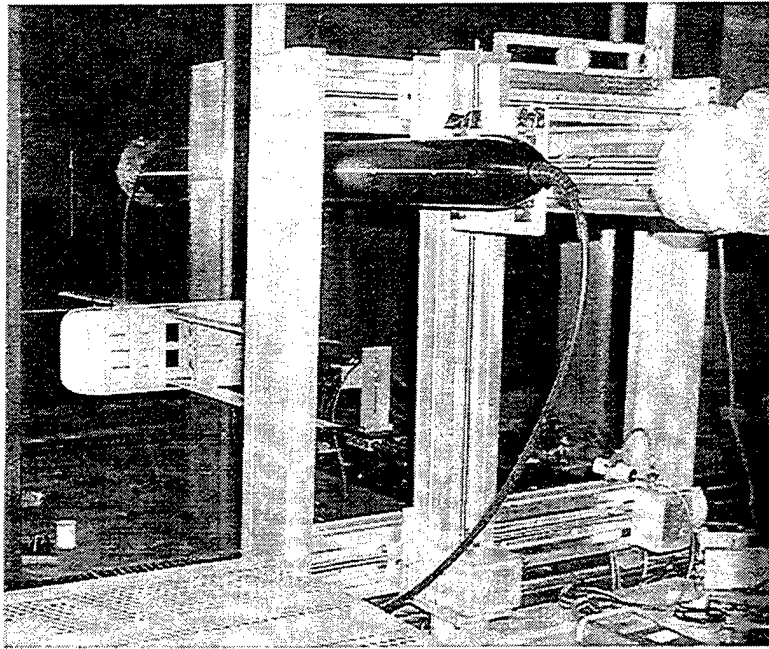
Figure 23. LDV Probe on 3-Axis Traverse at Test Section Window.

APPENDIX D. WIND TUNNEL CALIBRATION

Following repair and refurbishment of the wind tunnel, a tunnel calibration was conducted using the LDV system and pitot-static tube. A general description of the LDV and pitot-static system can be found in the Experimental Apparatus section. A detailed description of the LDV is found in Appendix C.

In preparation for calibration, the model and other associated equipment were removed from the tunnel. Measurements were taken over the tunnel velocity range of 0 to 9.5 m/s by both the pitot-static tube and the LDV probe. The data was used to plot a curve comparing the LDV to pitot measurements. Turbulence intensity was recorded by the LDV for plotting as well. The last recorded evaluation of the turbulence intensity was performed by Costello [Ref. 19] with hot-wire anemometers. In the velocity range of 1.8 to 9.8 m/s, he recorded a turbulence intensity range from 0.47% to 0.97%. A 750 mm focal length LDV lens will be acquired soon, allowing LDV measurements to the center of the tunnel, and an expanded turbulence intensity evaluation.

The newly installed pitot tube is located approximately 2.5 m upstream of the model and LDV probe. The tube is 0.75 m above the tunnel floor, and can be traversed in and out of the flow, from 0 to 0.5 m across the tunnel. Further downstream, the LDV is mounted outside the tunnel on a 3-axis traverse mechanism abeam the model's usual position, labeled as test section in Figure 13.

An MKS Baratron type 223B differential pressure transducer connected to the pitot-static probe. The transducer voltage output is linear with pressure. Bernoulli's equation was used to relate the pitot-static pressure to velocity:

$$V_{pitot} = \sqrt{\frac{2\Delta P}{\rho_\infty}} \qquad (25)$$

where V_{pitot} is flow velocity as measured by the pitot-static tube, ΔP is the pitot-static pressure differential, and ρ is atmospheric density.

For the first experiment, the LDV was moved from its normal position at the test section window to a plexiglass window that the pitot tube is mounted in. The two were essentially co-located, with the LDV probe 0.1 m above and 0.05 m in front of the pitot

tube. Both were positioned to take velocity measurements approximately 0.35 m from the tunnel wall, the range limit of the current LDV probe lens. LDV and pitot-static measurements were simultaneously taken and recorded for comparison. Pitot voltages were recorded by a digital voltmeter for 60 seconds, the time found to allow for consistent velocity convergence. The LDV measurement runs consisted of 5,000 samples taken over a period of 5 to 15 seconds, dependent upon smoke density. Pitot voltages and LDV free-stream velocity and associated velocity fluctuations were recorded for subsequent data reduction.

Three curves were produced. The LDV velocity as a function of pitot-static voltage output is shown in Figure 24. Figure 25 is a linear fit of LDV and pitot velocity using the experimental data fit equation from Figure 24. Figure 26 plots the tunnel turbulence intensity versus tunnel velocity as recorded by the LDV. The turbulence level remained below 3.3% above 2 m/s. Tabular data is attached at the end of the Appendix.
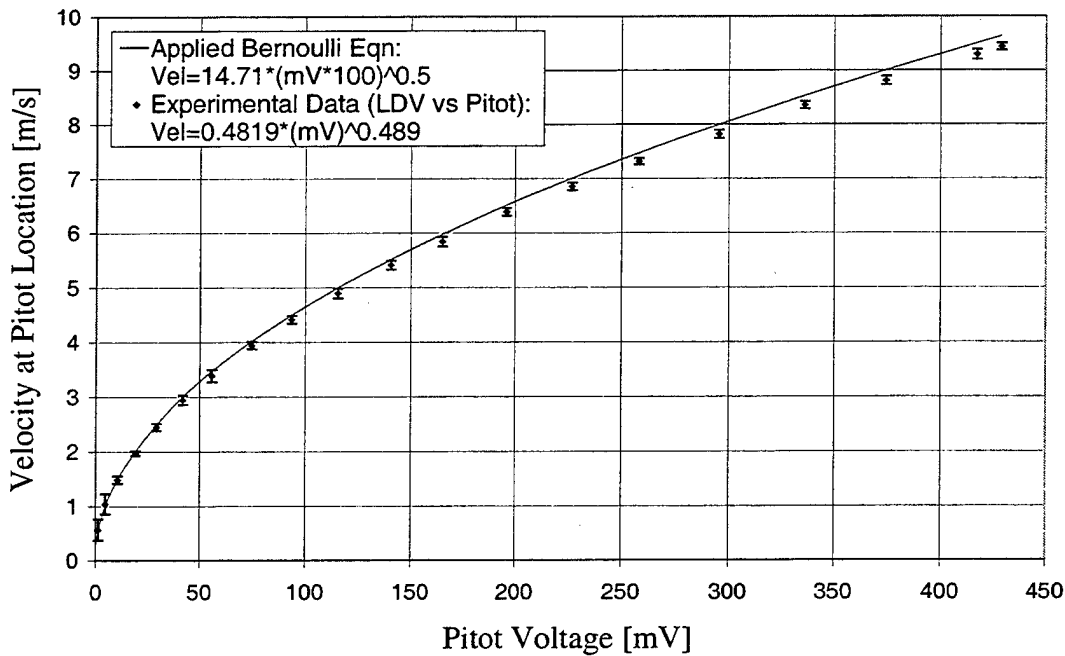
Figure 24. LDV Velocity vs Pitot Voltage (LDV, Pitot Co-located).
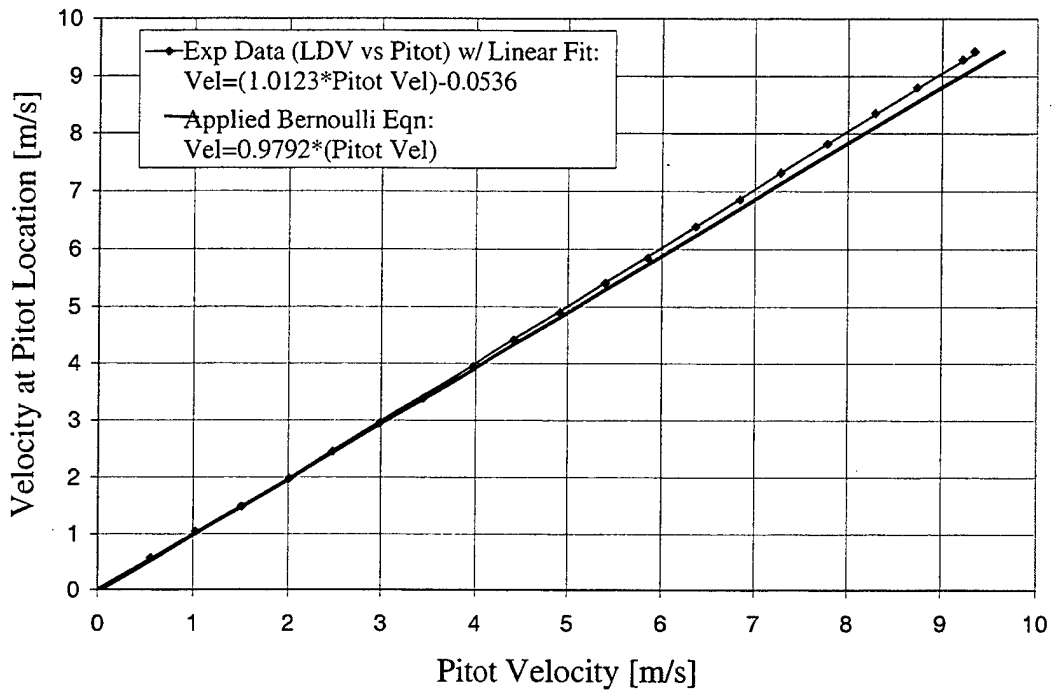
Figure 25. LDV vs Pitot-Static Velocity (LDV, Pitot Co-located).
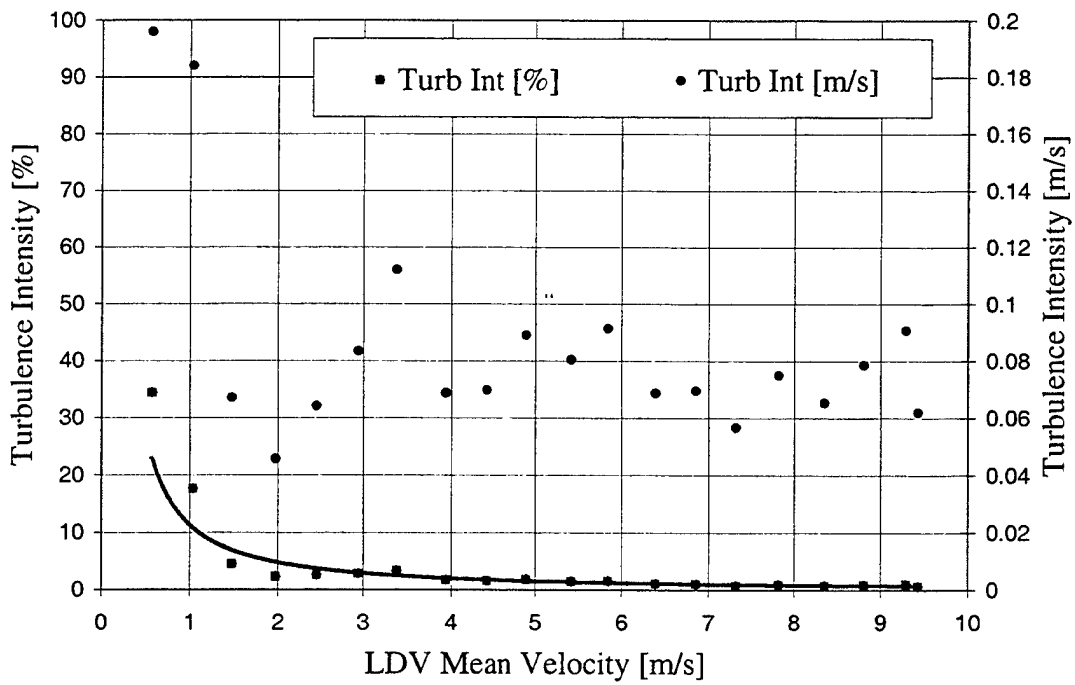
Figure 26. Turbulence Intensity vs LDV Velocity (LDV, Pitot Co-located).

In the second experiment, the LDV probe was mounted on its traverse, 2.4 m downstream from the pitot-static tube. The pitot-static tube remained at its fixed height of 0.75 m, with the LDV 0.1 m lower. Both were positioned to obtain the velocity 0.35 m from the tunnel wall. The tunnel cross-section is nominally 1.5 x 1.5 m, but does expand 2.6% over the 2.4 m between the pitot-static tube and LDV probe. It is assumed this was designed in to account for boundary layer growth.

The first experiment's procedures were repeated with the LDV at the test section. LDV velocities were lower than the pitot-static velocities, as would be expected due to the expanding area. Figure 27 shows the LDV velocity as a function of pitot-static voltage. Figure 28 is a near-linear fit of LDV and pitot velocity using the equation from Figure 27. Figure 29 presents the LDV recorded turbulence intensity at the position normally occupied by the model. The turbulence level remained below 1.75% above 1.5 m/s. In general, the intensity levels at the two tunnel positions were comparable. Tabular data follows the figures.
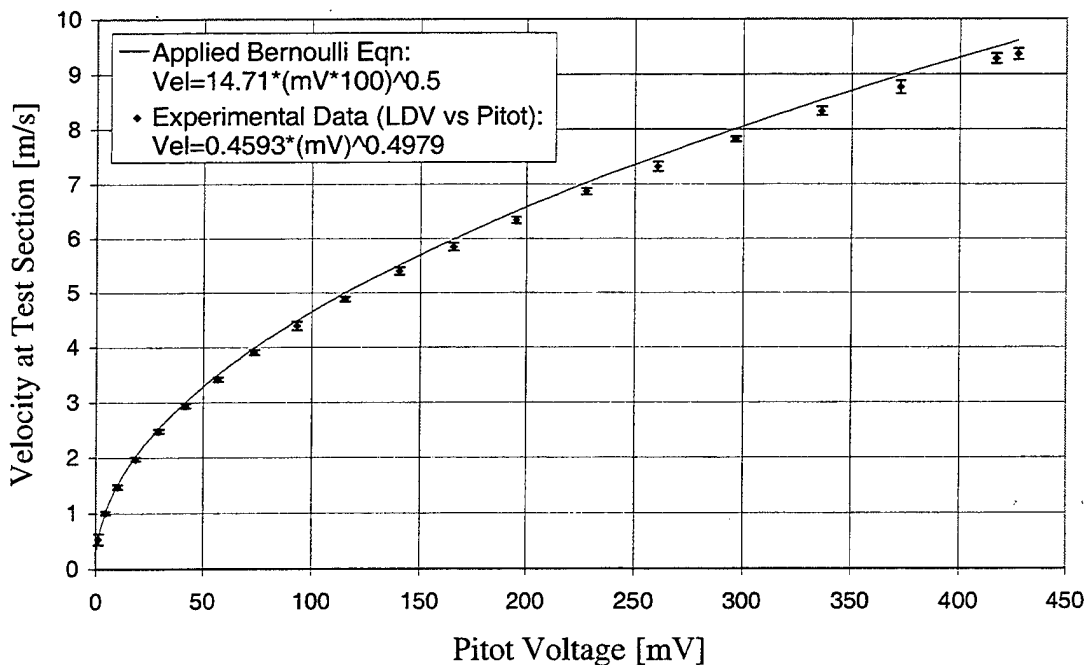
Figure 27. LDV Velocity vs Pitot Voltage (LDV downstream of pitot at Test Section).
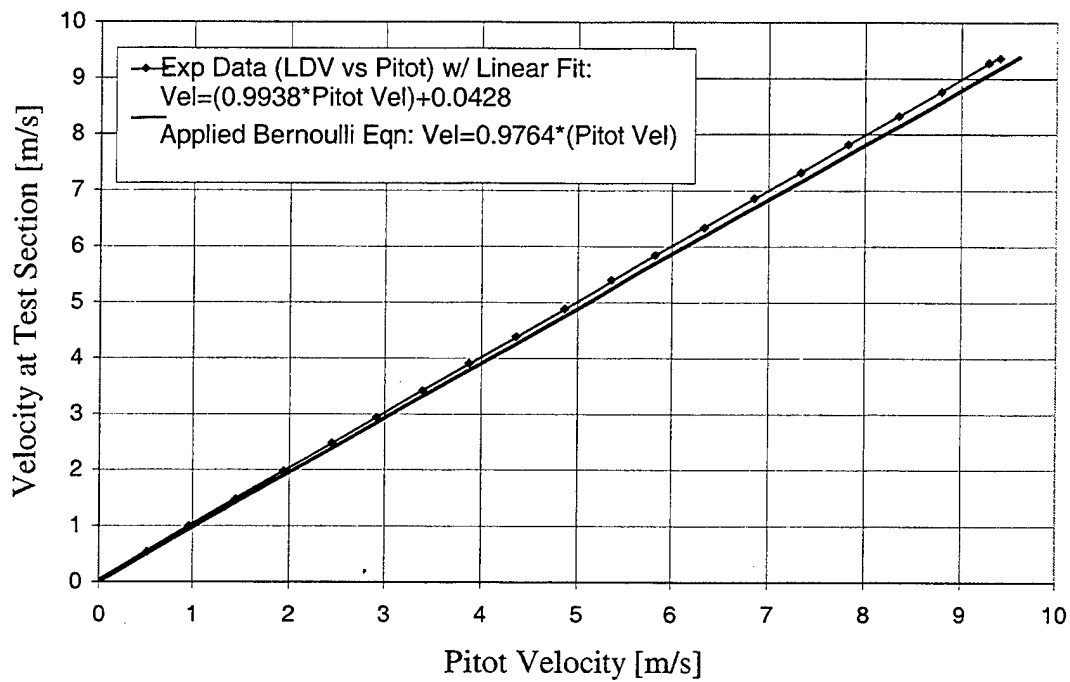
Figure 28. LDV vs Pitot-Static Velocity (LDV downstream of pitot at test section).
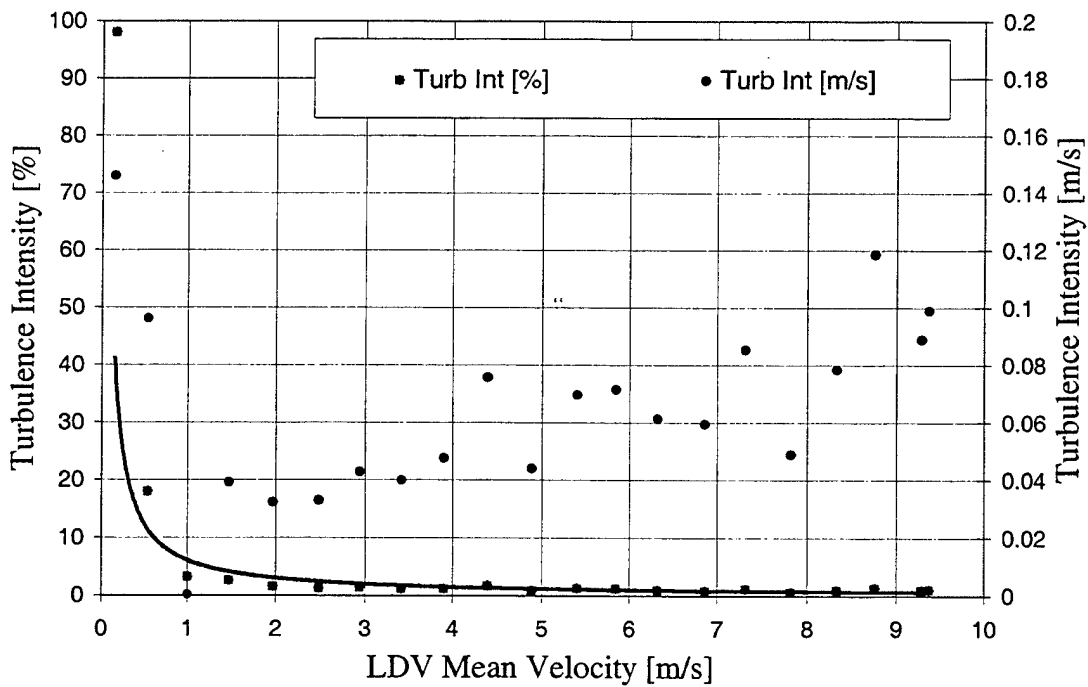
Figure 29. Turbulence Intensity vs LDV Velocity at Test Section.

Pitot/LDV Co-located

Run	Sample Size	LDV Mean Velocity [m/s]	Vel Std Dev [m/s]	Turbulence Intensity [%]	Turbulence Intensity [m/s]	Pitot (60 s mean) [mV], [V]	Pitot (60 s mean) [mV]	Pitot Vel fm Eqn 1 [m/s]	Pitot Vel fm Eqn 2 [m/s]
1	2000	-0.060	0.049	81.94	-0.049	-0.223	-0.223	#NUM!	#NUM!
2	2000	0.569	0.196	34.42	0.196	1.318	1.318	0.534	0.552
3	2000	1.041	0.184	17.68	0.184	4.721	4.721	1.011	1.029
4	5000	1.488	0.067	4.50	0.067	10.330	10.330	1.495	1.510
5	5000	1.974	0.046	2.31	0.046	18.590	18.590	2.006	2.012
6	5000	2.451	0.064	2.61	0.064	28.713	28.713	2.493	2.489
7	5000	2.944	0.083	2.83	0.083	41.758	41.758	3.006	2.989
8	5000	3.387	0.112	3.31	0.112	55.744	55.744	3.473	3.442
9	5000	3.943	0.069	1.74	0.069	74.715	74.715	4.021	3.972
10	5000	4.413	0.070	1.58	0.070	93.437	93.437	4.496	4.431
11	5000	4.895	0.089	1.82	0.089	115.434	115.434	4.998	4.914
12	5000	5.411	0.080	1.49	0.080	140.493	140.493	5.514	5.410
13	5000	5.840	0.091	1.57	0.091	165.057	165.057	5.976	5.853
14	5000	6.388	0.069	1.08	0.069	195.931	195.931	6.511	6.365
15	5000	6.854	0.070	1.01	0.070	0.227	226.898	7.007	6.838
16	5000	7.315	0.057	0.77	0.057	0.258	258.016	7.472	7.282
17	5000	7.820	0.075	0.96	0.075	0.295	295.475	7.996	7.781
18	5000	8.356	0.065	0.78	0.065	0.336	336.066	8.528	8.287
19	5000	8.807	0.079	0.89	0.079	0.374	374.441	9.001	8.737
20	5000	9.291	0.091	0.98	0.091	0.417	416.852	9.497	9.207
21	5000	9.433	0.062	0.66	0.062	0.429	428.836	9.633	9.336
Eqn 1=14.71*(volts)^.5			Eqn 1 based on Bernoulli						
Eqn 2=0.4819(mV)^0.489			Eqn 2 derived fm experimental data						

Table 4. Velocity Data for Pitot-LDV Co-located.

LDV on Traverse (downstream)

Run	Sample Size	LDV Mean Velocity [m/s]	Vel Std Dev [m/s]	Turbulence Intensity [%]	Turbulence Intensity [m/s]	Pitot (60 s mean) [mV], [V]	Pitot (60 s mean) [mV]	Pitot Vel fm Eqn 1 [m/s]	Pitot Vel fm Eqn 2 [m/s]
22	5000	0.149	0.149	98.091	0.146	-0.14	-0.14	#NUM!	#NUM!
23	5000	0.534	0.096	17.994	0.096	1.36	1.36	0.543	0.518
24	5000	1.003	1.003	0.033	0.000	4.67	4.67	1.005	0.964
25	5000	1.472	0.039	2.662	0.039	10.50	10.50	1.507	1.451
26	5000	1.973	0.032	1.638	0.032	18.79	18.79	2.017	1.946
27	5000	2.478	0.033	1.330	0.033	29.49	29.49	2.526	2.442
28	5000	2.941	0.043	1.457	0.043	41.71	41.71	3.004	2.909
29	5000	3.417	0.040	1.167	0.040	56.87	56.87	3.508	3.402
30	5000	3.906	0.048	1.218	0.048	73.64	73.64	3.992	3.876
31	5000	4.390	0.076	1.725	0.076	93.10	93.10	4.488	4.362
32	5000	4.884	0.044	0.901	0.044	115.46	115.46	4.998	4.863
33	5000	5.398	0.070	1.290	0.070	140.10	140.10	5.506	5.361
34	5000	5.841	0.071	1.224	0.071	165.50	165.50	5.984	5.832
35	5000	6.333	0.061	0.968	0.061	195.04	195.04	6.496	6.335
36	5000	6.861	0.059	0.866	0.059	0.23	228.08	7.025	6.856
37	5000	7.321	0.085	1.166	0.085	0.26	260.22	7.504	7.327
38	5000	7.823	0.049	0.624	0.049	0.30	296.44	8.009	7.825
39	5000	8.331	0.078	0.941	0.078	0.34	336.43	8.532	8.341
40	5000	8.764	0.119	1.353	0.119	0.37	372.85	8.982	8.785
41	5000	9.280	0.089	0.958	0.089	0,42	416.50	9.493	9.290
42	5000	9.365	0.099	1.057	0.099	0.43	426.85	9.611	9.405
Eqn 1=14.71*(volts)^.5			Eqn 1 based on Bernoulli						
Eqn 2=0.443(mV)^0.5045			Eqn 2 derived fm experimental data						

Table 5. Velocity Data for Pitot-LDV with LDV at Test Section.

APPENDIX E. MODEL THRUST/WEIGHT CALIBRATION

Weight vs Voltage Calibration									
					Weight [g], [N]				
[g]	0	3	5	10	20	35	50	65	75
[N]	0.0000	0.0294	0.0490	0.0981	0.1961	0.3432	0.4903	0.6374	0.7355
Run a mean [V]	0.0041	0.0877	0.1402	0.2603	0.5192	0.8966	1.2710	1.6630	1.9240
Run a std dev [V]	0.0014	0.0005	0.0006	0.0010	0.0007	0.0006	0.0006	0.0007	0.0008
Run b mean [V]	0.0047	0.0851	0.1383	0.2539	0.5168	0.9026	1.2901	1.6682	1.9351
Run b std dev [V]	0.0059	0.0007	0.0006	0.0008	0.0010	0.0011	0.0015	0.0010	0.0011
Run c mean [V]	0.0060	0.0875	0.1389	0.2575	0.5169	0.8951	1.2862	1.6686	1.9203
Run c std dev [V]	0.0043	0.0012	0.0009	0.0009	0.0009	0.0010	0.0008	0.0007	0.0006
Avg Voltage [V]	0.0049	0.0868	0.1391	0.2572	0.5176	0.8981	1.2824	1.6666	1.9265
Avg Distance [mm]	0.0495	0.8678	1.3914	2.5723	5.1764	8.9810	12.8244	16.6659	19.2649
Avg Std Dev [V]	0.0039	0.0008	0.0007	0.0009	0.0009	0.0009	0.0010	0.0008	0.0008
Corrected Voltage [V]	0.0000	0.0818	0.1342	0.2523	0.5127	0.8932	1.2775	1.6616	1.9215
Thrust fm eqn	0.0000	0.0314	0.0514	0.0967	0.1965	0.3423	0.4897	0.6369	0.7365
Error [%]	#DIV/0!	6.6135	4.9034	1.3925	0.1951	0.2578	0.1366	0.0820	0.1398

Table 6. Thrust Calibration Table.
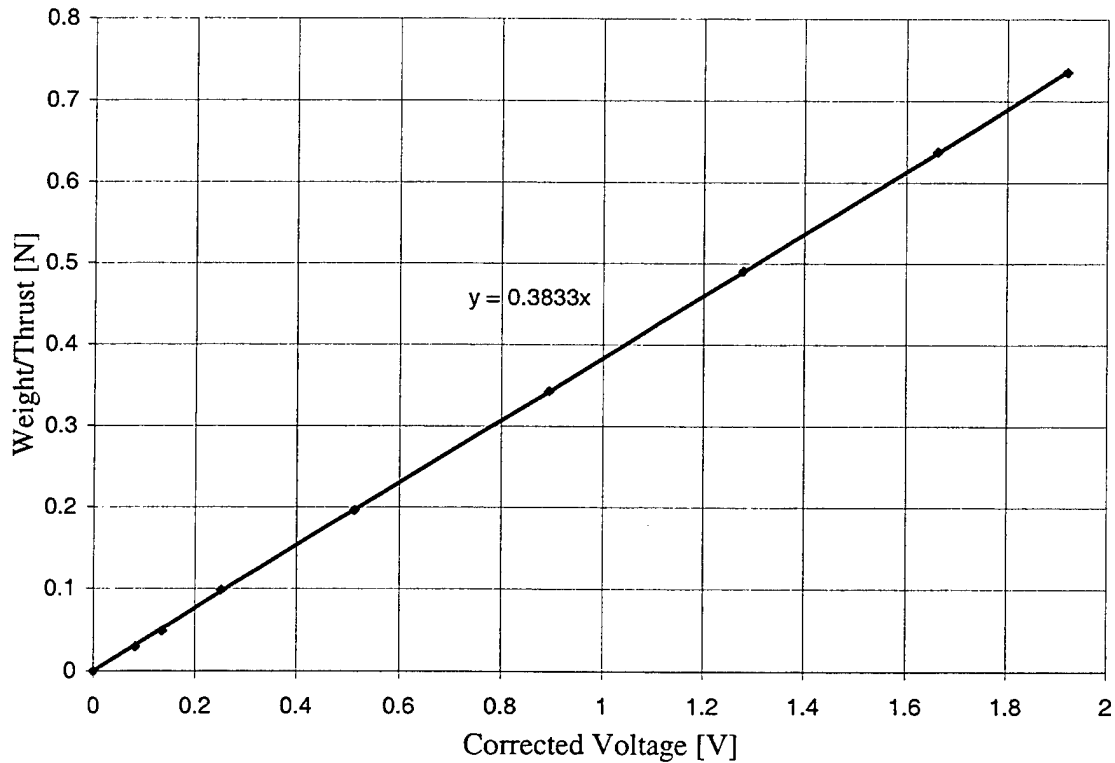
Figure 30. Thrust Calibration Curve.

THIS PAGE INTENTIONALLY LEFT BLANK

APPENDIX F. MATLAB PROGRAM FOR DSO-2102 OSCILLOSCOPE DATA REDUCTION

```
% LT T.C. Lund
% DSO-2102 PC Oscilloscope data conversion program
% Filename:  Convert.m

% This program converts data saved from the DSO-2102 oscilloscope
% software into voltage, range, thrust, and frequency.  It converts
% and saves only the first two columns of the .prn file type, but
% could easily be modified to read all six columns, or to read the
% .csb or .csv data file types.

% For program users:
% - When you take your data, save your .prn files as a filename of
%   less than eight characters total, with the last characters as
%   sequential numbers (e.g. thrst100.prn, thrst101.prn, etc).
% - Enter the data under "Fill in this part."
% - Output goes to filename.wri (e.g. thrst100.wri, thrst101.wri) and
%   Mean_Thrust.wri (Caution:  The program deletes existing
%   filename.wri and Mean_Thrust.wri files). The programs open in
%   Wordpad for quick viewing, but the cols will be out of alignment.
%   The output is designed for Excel, where the cols will be aligned.
% - You also must update the following eqns with each configuration:
%   1. The 5 eqns that convert voltage to thrust.
%   2. The 1 eqn for weight calibration error.
% - Program assumes you select +/-5V on laser rangefinder (not 0-10V)
% - Program assumes range data goes into DSO Chan B, and trip switch
%   goes into DSO Chan A.
% - Program assumes that the frequency trip switch is a negative
%   voltage.  See notes under DSO data variables and 3rd if statement.
clear
delete Mean_Thrust.wri;
% ****************** Fill in this part ****************************
filename='thrst';
filetype='.prn';
startfilenumber=100;           % First file number
lastfilenumber=163;            % Last file number
voltsperdiv=.2;                % Volts per division fm DSO
sample_rate=1000;              % Sample rate in Hz fm DSO
v_zero=.00251;                 % DSO zero voltage offset
% ****************************************************************
fid1 = fopen('Mean_Thrust.wri','w');
fprintf(fid1,'Filename\tVel\tVel\tMean\tCorrected\tTotal Error\t');
fprintf(fid1,'Avg Dev\tLaser\tDSO\tWt Cal\tMean\tAvg Dev\tMin\tMax\n');
fprintf(fid1,'\t\tStd Dev\tThrust\tThrust\t+/-\tError\tError\tError\t');
fprintf(fid1,'Error\tFrequency\tFrequency\tFrequency\tFrequency\n');
fprintf(fid1,'\t[m/s]\t[m/s]\t[N]\t[N]\t[N]\t[N]\t[N]\t[N]\t[N]\t');
fprintf(fid1,'[Hz]\t[Hz]\t[Hz]\t[Hz]\n\n');
fclose(fid1);
for i=100:lastfilenumber
    clear data              % Clears data matrix each iteration
```

```
% ********************** Loads data *********************************
disp(['******* Computing ',filename,num2str(i),filetype,' *******'])
rawdata=load ([filename,num2str(i),filetype]);
data(:,1)=rawdata(:,2); % CH B is loaded to data col 1
data(:,8)=rawdata(:,1); % CH A is loaded to data col 8
% ******** Converts data to voltage and distance (1V=1cm) **********
data(:,2)=(voltsperdiv*5.12)-((data(:,1))*(voltsperdiv*10.24/256));
data(:,9)=(voltsperdiv*5.12)-((data(:,8))*(voltsperdiv*10.24/256));
% ******** Voltage correction **************************************
data(:,3)=data(:,2)+v_zero; % DSO volts corrected for Vzero offset
% ******** Converts voltage to thrust [N] **************************
data(:,5)= 0.3833* data(:,3);
% ******** Computes the avg dev of thrust & freq in data ***********
% DSO data variables
sig_trip = 175;        % The minimum data value that trips micro-switch
sig_old1 = 257;        % sig_old1, 2, and 3 are the 3 data points prior
sig_old2 = 257;        % to the current pt. Use 257 if the trip signal
sig_old3 = 257;        % is neg voltage. Use -1 if trip is a + voltage.
% Voltage variables
cycle_volts=0;         % Sum of voltage for one cycle
cycle_mean_volts=0;    % Mean volts of one cycle
volts_sum=0;           % Sum of voltages of all cycles
% Thrust variables
cycle_thrust=0;        % Sum of thrust for one cycle
cycle_mean_thrust=0;   % Mean thrust of one cycle
thrust_sum=0;          % Sum of mean thrust of all cycles
% Frequency variables
cycle_mean_freq=0;     % Mean frequency of one cycle
freq_sum=0;            % Sum of frequencies of all cycles
freq=0;                % Variable for min frequency
k=1;                   % Min freq counter
% Counter variables
nr_cycles=-1;          % Counter for total number of cycles in data
cycle_data_pts=0;      % Number of data pts within one cycle
total_data_pts=0;      % Number of data pts of all cycles
data_points=length(data(:,1)); % Counts rows of data matrix
for j=1:data_points  % Looks at all data points
   if abs(data(j,2)) > 5
      error ('** Voltage is outside rangefinder limits (+/- 5V) **')
   end
   if nr_cycles >= 0 % Ignores partial data before 1st cycle
      cycle_volts = cycle_volts + data (j-1,2); % Sums cycle volts
      cycle_thrust = cycle_thrust + data(j-1,5); % Sums cycle thrust
      cycle_data_pts=cycle_data_pts+1; % Counts data pts in cycle
   end
   % Is micro-switch tripped?
   if data(j,8)>=sig_trip & sig_old1<sig_trip & ...
         sig_old2<sig_trip & sig_old3<sig_trip % This assumes a neg
         % trip voltage. Change >, < signs if trip is a + voltage.
      nr_cycles=nr_cycles+1;   % Count only when ifs met
      if nr_cycles > 0 % Ignores partial data before 1st cycle
         % Volts
         cycle_mean_volts=cycle_volts/cycle_data_pts; % Cycle mean
         data(j-1,4)=cycle_mean_volts; % Stores cycle mean volts
```

62

```matlab
            volts_sum=volts_sum+cycle_mean_volts; % Sums total volts
            % Thrust
            cycle_mean_thrust=cycle_thrust/cycle_data_pts; % Cycle mean
            data(j-1,6)=cycle_mean_thrust; % Stores cycle mean thrust
            thrust_sum=thrust_sum+cycle_mean_thrust; % Sums tot thrust
            % Frequency
            cycle_mean_freq=sample_rate/cycle_data_pts; % Cycle mean
            data(j-1,7)=cycle_mean_freq; % Stores cycle mean frequency
            freq_sum=freq_sum+cycle_mean_freq; % Sums all cycle freqs
            if data(j-1,7)>0
                freq(k) = cycle_mean_freq;  % Save nonzero freqs
                k=k+1;
            end
            total_data_pts=total_data_pts+cycle_data_pts;
            % Reset variables
            cycle_volts=0;              % Reset cycle voltage for new cycle
            cycle_thrust=0;   % Reset thrust summation for new cycle
            cycle_freq=0;             % Reset freq summation for new cycle
            cycle_data_pts=0; % Reset nr of data pts for new cycle
        end
    end
    sig_old1 = data(j,8);      % Last signal value
    if j>=3
        sig_old2 = data(j-1,8); % The data value before the last one
        sig_old3 = data(j-2,8); % Three data points back
    end
end
% Voltage and frequency calculations:
volts_mean=volts_sum/nr_cycles;
if volts_mean==0         % No or very slow flap case, still need data
    volts_mean=mean(data(:,3));
end
inner_sum1=0;  % Inner summation for adev of volts
inner_sum2=0;  % Inner summation for adev of freq
freq_mean=freq_sum/nr_cycles; % Mean freq of cycles
max_freq=max(freq); % Max cycle freq of all cycles
min_freq=min(freq); % Min cycle freq of all cycles
for m=1:data_points
    if data(m,6)>0
        inner_sum1=inner_sum1 + abs(data(m,4)-volts_mean);
        inner_sum2=inner_sum2 + abs(data(m,7)-freq_mean);
    end
end
adev_freq=inner_sum2/nr_cycles; % Avg dev of frequency
% Thrust
thrust_mean=0.3833*volts_mean; % Mean thrust of cycles
% *** There are 4 sources of thrust error:
% *** 1st one is due to cyclic nature of flapping-wing thrust: *****
adev_volts=inner_sum1/nr_cycles; % adev fm voltage data
% *** 2nd source of error - laser rangefinder error [mm] **********
if abs(volts_mean) < 3.5
    error_laser = 0.1 + 0.002 * abs(10 * volts_mean);
else
    error_laser = 0.25 + 0.005 * abs(10 * volts_mean);
```

```
  end
  error_laser = error_laser/10; % Convert range error to volts error
  % *** Oscilloscope volt max error=resolution of DSO-2102-3rd error *
  error_DSO = (voltsperdiv*5.12)/128;
  % *** Convert errors fm voltage to thrust [N] error ****************
  adev_thrust1=0.3833*adev_volts;
  error_thrust2=0.3833*error_laser;
  error_thrust3=0.3833*error_DSO;
  % *** Computes adev due to weight calibration - 4th error: *********
  thrust_hi= 0.3836*volts_mean - 3E-06;
  error_thrust4 = thrust_hi-thrust_mean;
  error_thrust=adev_thrust1+error_thrust2+error_thrust3+error_thrust4;
  % **************** Saves all data to filename.wri *****************
  filesave2=([filename,num2str(i),'.wri']);
  fid2 = fopen(filesave2,'w');
  fprintf(fid2,[filename,num2str(i)]);
  fprintf(fid2,'\nCH B\tCH B\tCH B\tCH B\tCH B\t');
  fprintf(fid2,'CH B\tCH B\tCH A\tCH A\n');
  fprintf(fid2,'Data\tVoltage\tAbsol Volt\tCycle Mean\tThrust\t');
  fprintf(fid2,'Cycle Mean\tFreq Mean\tData\tVoltage\n');
  fprintf(fid2,'\t[V],[cm]\t[V],[cm]\t[V]\t[N]\t[N]\t');
  fprintf(fid2,'[Hz]\t\t[V]\n');
  fprintf(fid2,'\n\tMean thrust =\t\t\t %10.8f',thrust_mean);
  fprintf(fid2,'\n\tThrust Avg Dev Error =\t\t\t %10.8f',adev_thrust1);
  fprintf(fid2,'\n\tLaser Error =\t\t\t %10.8f',error_thrust2);
  fprintf(fid2,'\n\tOscilloscope Error =\t\t\t %10.8f',error_thrust3);
  fprintf(fid2,'\n\tWt/Thrust Cal Error =\t\t\t %10.8f',error_thrust4);
  fprintf(fid2,'\n\tTotal Error =\t\t\t %10.8f',error_thrust);
  fprintf(fid2,'\n\t\t\t\tMean frequency =\t\t %4.2f\n',...
      freq_mean);
  fprintf(fid2,'\t\t\t\tAvg Dev =\t\t %4.2f\n',adev_freq);
  fprintf(fid2,'\t\t\t\tMin Freq =\t\t %4.2f\n',min_freq);
  fprintf(fid2,'\t\t\t\tMax Freq =\t\t %4.2f\n\n',max_freq);
  fprintf(fid2,'%3.0f\t %4.3f\t %5.4f\t %5.4f\t %8.5f\t %8.5f\t %5.2f\t
      %3.0f\t %4.3f\n',data.');
  fclose(fid2);
  % ************ Saves summary of data to Mean_Thrust.wri **********
  fid3 = fopen('Mean_Thrust.wri','a');
  fprintf(fid3,[filename,num2str(i)]);
  fprintf(fid3,'\t\t\t%10.8f\t\t%10.8f\t\t%10.8f\t%10.8f\t%10.8f\t
      %10.8f\t%4.2f\t%4.2f\t%4.2f\t%4.2f\n',...
      thrust_mean,error_thrust,adev_thrust1,error_thrust2,error_thrust3,...
      error_thrust4,freq_mean,adev_freq,min_freq,max_freq);
  fclose(fid3);
end
disp(['********* Program Complete **********'])
```

APPENDIX G. EXPERIMENTAL DATA

Data sorted by flapping frequency (0, 3, 5, 7 Hz)

Filename	Velocity		Thrust							Frequency				
	Vel	Vel St Dev	Mean Thrust	Corrected Thrust	Total Error +/-	Avg Dev Error	Laser Error	DSO Error	Wt Cal Error	Mean Freq	Avg Dev Freq	Min Freq	Max Freq	Red freq k
	[m/s]	[m/s]	[N]	[N]	[N]	[N]	[N]	[N]	[N]	[Hz]	[Hz]	[Hz]	[Hz]	
thrst100	0	0	-0.00016	0	0.00690	0.00000	0.00383	0.00307	0.00000	0	0	0	0	
thrst104	0.57	0.06	-0.00170	0	0.00690	0.00000	0.00384	0.00307	0.00000	0.11	0	0.11	0.11	
thrst108	0.99	0.06	-0.00121	0	0.00700	0.00010	0.00384	0.00307	0.00000	0.14	0	0.14	0.14	
thrst112	1.51	0.05	-0.00244	0	0.00690	0.00000	0.00384	0.00307	0.00000	0.13	0	0.13	0.14	
thrst116	2.08	0.03	-0.00001	0	0.00690	0.00001	0.00383	0.00307	0.00000	0.08	0	0.08	0.08	
thrst120	2.48	0.03	-0.00074	0	0.00698	0.00008	0.00383	0.00307	0.00000	0.11	0	0.11	0.11	
thrst124	2.98	0.06	-0.00169	0	0.00690	0.00000	0.00384	0.00307	0.00000	0.1	0	0.09	0.1	
thrst128	3.50	0.05	-0.00187	0	0.00690	0.00000	0.00384	0.00307	0.00000	0.09	0	0.09	0.09	
thrst132	3.99	0.06	-0.00436	0	0.00690	0.00000	0.00384	0.00307	-0.00001	0.1	0	0.1	0.1	
thrst136	4.54	0.06	0.00184	0	0.00743	0.00053	0.00384	0.00307	0.00000	0.11	0	0.11	0.11	
thrst140	4.99	0.07	-0.00166	0	0.00690	0.00000	0.00384	0.00307	0.00000	0.12	0	0.12	0.12	
thrst144	6.01	0.06	-0.00950	0	0.00691	0.00000	0.00385	0.00307	-0.00001	0.12	0	0.12	0.12	
thrst148	7.01	0.05	-0.00397	0	0.00690	0.00000	0.00384	0.00307	-0.00001	0.1	0	0.1	0.1	
thrst152	7.99	0.07	-0.01851	0	0.00692	0.00000	0.00387	0.00307	-0.00002	0.08	0	0.08	0.08	
thrst156	9.01	0.07	0.00984	0	0.00776	0.00084	0.00385	0.00307	0.00000	0.11	0	0.1	0.11	
thrst160	9.47	0.08	0.00758	0	0.00841	0.00149	0.00385	0.00307	0.00000	0.09	0	0.09	0.1	
thrst101	0	0	0.00703	0.00719	0.00821	0.00000	0.00385	0.00307	0.00000	2.95	0	2.93	2.96	#DIV/0!
thrst105	0.57	0.06	0.00712	0.00881	0.00991	0.00300	0.00385	0.00307	0.00000	2.93	0	2.92	2.95	2.08
thrst109	0.99	0.06	0.00863	0.00984	0.00750	0.00058	0.00385	0.00307	0.00000	2.96	0	2.95	2.98	1.20
thrst113	1.51	0.05	0.01140	0.01385	0.00948	0.00255	0.00386	0.00307	0.00001	2.94	0	2.93	2.95	0.78
thrst117	2.08	0.03	0.01246	0.01246	0.00954	0.00260	0.00386	0.00307	0.00001	2.94	0.01	2.92	2.95	0.57
thrst121	2.48	0.03	0.01054	0.01128	0.00929	0.00236	0.00385	0.00307	0.00001	2.94	0	2.93	2.95	0.48
thrst125	2.98	0.06	0.00990	0.01159	0.01003	0.00311	0.00385	0.00307	0.00000	2.95	0	2.93	2.96	0.40
thrst129	3.50	0.05	0.00862	0.01050	0.01037	0.00345	0.00385	0.00307	0.00000	2.95	0	2.94	2.97	0.34
thrst133	3.99	0.06	0.01199	0.01635	0.01255	0.00562	0.00386	0.00307	0.00001	2.95	0	2.94	2.96	0.30
thrst137	4.54	0.06	0.02272	0.02089	0.01501	0.00805	0.00388	0.00307	0.00001	2.96	0.01	2.95	2.98	0.26
thrst141	4.99	0.07	0.02249	0.02416	0.01085	0.00389	0.00388	0.00307	0.00001	2.96	0	2.95	2.97	0.24
thrst145	6.01	0.06	0.03372	0.04322	0.01091	0.00392	0.00390	0.00307	0.00002	2.97	0	2.95	2.99	0.20
thrst149	7.01	0.05	0.05019	0.05416	0.01043	0.00339	0.00393	0.00307	0.00004	2.95	0	2.94	2.97	0.17
thrst153	7.99	0.07	0.05486	0.07337	0.01413	0.00708	0.00394	0.00307	0.00004	2.94	0	2.93	2.96	0.15
thrst157	9.01	0.07	0.08894	0.07910	0.01296	0.00581	0.00401	0.00307	0.00007	2.95	0.01	2.93	2.97	0.13
thrst161	9.47	0.08	0.08224	0.07466	0.01691	0.00978	0.00400	0.00307	0.00006	2.95	0.01	2.94	2.97	0.13
thrst102	0	0	0.02155	0.02171	0.01010	0.00314	0.00388	0.00307	0.00001	5	0.01	4.98	5.03	#DIV/0!
thrst106	0.57	0.06	0.02829	0.02998	0.00943	0.00245	0.00389	0.00307	0.00002	4.96	0.01	4.93	5	3.51
thrst110	0.99	0.06	0.02480	0.02602	0.00750	0.00053	0.00388	0.00307	0.00002	5.03	0.01	5	5.05	2.03
thrst114	1.51	0.05	0.02788	0.03032	0.00771	0.00074	0.00389	0.00307	0.00002	5	0.01	4.98	5.03	1.33
thrst118	2.08	0.03	0.03794	0.03795	0.00901	0.00201	0.00391	0.00307	0.00003	4.99	0.01	4.95	5.03	0.97
thrst122	2.48	0.03	0.04486	0.04560	0.00965	0.00263	0.00392	0.00307	0.00003	5	0.01	4.98	5.03	0.81
thrst126	2.98	0.06	0.05138	0.05308	0.00999	0.00295	0.00394	0.00307	0.00004	5	0.01	4.95	5.05	0.68
thrst130	3.50	0.05	0.05471	0.05659	0.01058	0.00353	0.00394	0.00307	0.00004	5.01	0.02	4.98	5.05	0.58
thrst134	3.99	0.06	0.06231	0.06667	0.01091	0.00384	0.00396	0.00307	0.00005	5.03	0.01	5	5.08	0.51
thrst138	4.54	0.06	0.07396	0.07213	0.01271	0.00560	0.00398	0.00307	0.00005	5.02	0.01	4.98	5.1	0.45
thrst142	4.99	0.07	0.07537	0.07703	0.00904	0.00194	0.00398	0.00307	0.00006	5	0.01	4.95	5.05	0.40
thrst146	6.01	0.06	0.09235	0.10185	0.01334	0.00619	0.00402	0.00307	0.00007	5.04	0.01	5	5.08	0.34
thrst150	7.01	0.05	0.11468	0.11865	0.01424	0.00703	0.00406	0.00307	0.00009	4.99	0.02	4.95	5.03	0.29
thrst154	7.99	0.07	0.12665	0.14516	0.01404	0.00679	0.00409	0.00307	0.00010	5.02	0.01	4.98	5.08	0.25
thrst158	9.01	0.07	0.17248	0.16265	0.01555	0.00817	0.00418	0.00307	0.00013	5.02	0.02	4.98	5.05	0.22
thrst162	9.47	0.08	0.17355	0.16597	0.01418	0.00680	0.00418	0.00307	0.00013	5.01	0.01	4.95	5.05	0.21
thrst103	0	0	0.04861	0.04877	0.01053	0.00350	0.00393	0.00307	0.00004	7.02	0.03	6.94	7.09	#DIV/0!
thrst107	0.57	0.06	0.04831	0.05001	0.01789	0.01086	0.00393	0.00307	0.00003	6.99	0.02	6.9	7.04	4.95
thrst111	0.99	0.06	0.05896	0.06017	0.01031	0.00325	0.00395	0.00307	0.00004	7.02	0.03	6.94	7.09	2.84
thrst115	1.51	0.05	0.05401	0.05645	0.00881	0.00176	0.00394	0.00307	0.00004	7.04	0.02	6.9	7.14	1.88
thrst119	2.08	0.03	0.06259	0.06260	0.00893	0.00186	0.00396	0.00307	0.00005	7.04	0.03	6.94	7.19	1.36
thrst123	2.48	0.03	0.07388	0.07462	0.01070	0.00360	0.00398	0.00307	0.00005	7.03	0.03	6.94	7.14	1.14
thrst127	2.98	0.06	0.09246	0.09415	0.01083	0.00368	0.00402	0.00307	0.00007	7.04	0.02	6.94	7.19	0.95
thrst131	3.50	0.05	0.11130	0.11317	0.01409	0.00689	0.00406	0.00307	0.00008	7.04	0.02	6.94	7.14	0.81
thrst135	3.99	0.06	0.13108	0.13545	0.01412	0.00686	0.00410	0.00307	0.00010	7.01	0.03	6.9	7.09	0.71
thrst139	4.54	0.06	0.15821	0.15638	0.01196	0.00463	0.00415	0.00307	0.00012	7.08	0.03	6.99	7.19	0.63
thrst143	4.99	0.07	0.16402	0.16568	0.01282	0.00547	0.00416	0.00307	0.00013	7.04	0.02	6.94	7.14	0.57
thrst147	6.01	0.06	0.19243	0.20194	0.01486	0.00743	0.00422	0.00307	0.00015	7.03	0.03	6.94	7.19	0.47
thrst151	7.01	0.05	0.22606	0.23003	0.01543	0.00791	0.00429	0.00307	0.00017	7.01	0.04	6.9	7.14	0.40
thrst155	7.99	0.07	0.24947	0.26798	0.01779	0.01020	0.00433	0.00307	0.00019	7.04	0.03	6.94	7.14	0.35
thrst159	9.01	0.07	0.30295	0.29311	0.02763	0.01989	0.00444	0.00307	0.00023	7.02	0.03	6.9	7.14	0.31
thrst163	9.47	0.08	0.31067	0.30309	0.01281	0.00505	0.00445	0.00307	0.00024	7.04	0.03	6.94	7.14	0.30

THIS PAGE INTENTIONALLY LEFT BLANK

LIST OF REFERENCES

1. Knoller, R., "Die Gesetze des Luftwiderstandes," *Flug- und Motortechnik* (Wien), Vol. 3, No. 21, 1909, pp. 1-7.

2. Betz, A., "Ein Beitrag zur Erklarung des Segelfluges," *Zeitschrift für Flugtechnik und Motorluftschiffahrt*, Vol. 3, Jan. 1912, pp. 269-272.

3. Katzmayr, R., "Effect of Periodic Changes of Angle of Attack on Behavior of Airfoils," NACA Report No. 147, Oct. 1922 (translated *from Zeitschrift für Flugtechnik und Motorluftschiffahrt*, March 31, 1922, pp. 80-82, and April 13, 1922, pp. 95-101).

4. Jones, K. D. and Platzer, M. F., "Numerical Computation of Flapping-Wing Propulsion and Power Extraction," AIAA Paper No. 97-0826, Reno, Nevada, January 1997.

5. Jones, K. D. and Platzer, M. F., "An Experimental and Numerical Investigation of Flapping-Wing Propulsion," AIAA Paper No. 99-0995, Reno, Nevada, January 1999.

6. Jones, K. D. and Platzer, M. F., "Flapping-Wing Propulsion for A Micro-Air Vehicle," AIAA Paper No. 2000-0897, Reno, Nevada, January 2000.

7. McCormick, B. W., *Aerodynamics, Aeronautics, and Flight Mechanics*, John Wiley & Sons, 1979, pp. 420-421, 523-524.

8. Teng, N. H., "The Development of a Computer Code for the Numerical Solution of Unsteady, Inviscid and Incompressible Flow over an Airfoil," Master's Thesis, Naval Postgraduate School, Monterey, California, June 1987.

9. Pang, C., "A Computer Code (USPOTF2) for Unsteady Incompressible Flow Past Two Airfoils," Master's Thesis, Naval Postgraduate School, Monterey, California, September 1988.

10. Hess, J.L. and Smith, A.M.O. "Calculation of Potential Flow about Arbitrary Bodies," *Progress in Aeronautical Sciences*, Vol. 8, Pergamon Press, Oxford, 1966, pp. 1-138.

11. Basu, B. C. and Hancock, G. J., "The Unsteady Motion of a Two –Dimensional Aerofoil in Incompressible Inviscid Flow," *Journal of Fluid Mechanics*, Vol. 87, 1978, pp. 159-168.

12. Bertin, J. J., Smith, M. L., *Aerodynamics for Engineers*, 3d edition, Prentice Hall, 1998, pp. 226, 266.

13. Schmidt, W., "Der Wellpropeller, ein neuer Antrieb fuer Wasser-, Land-, and Luftfahrzeuge," Z. Flugwiss. Vol. 13, 1965, pp. 472-479.

14. Ringleb, F. O., "The Three-Dimensional Smoke Tunnel of the Naval Air Engineering Laboratory in Philadelphia." Report. NAEL-ENG-6818, July 1961.

15. Chandrasekhara, M. S., Advanced Aeronautical Laboratory Class Lecture Notes, Naval Postgraduate School, Monterey, California, April 1999.

16. Press, W. H., Flannery B. P., Teukolsky, S. A., Vetterling, W. T., *Numerical Recipes*, Cambridge University Press, 1989, pp. 455, 456.

17. Instruction Manual, *Model IFA 550 Signal Processor*, TSI Incorporated, April 1996, p. 4-19.

18. Instruction Manual, *Model IFA 755 Digital Burst Correlator*, TSI Incorporated, January 1999, p. 1-3.

19. Costello, J. P. II, "Smoke and Helium Bubble Visualization Studies of Incompressible Flow Past a Jet-Flap Airfoil," Master's Thesis, Naval Postgraduate School, Monterey, California, June 1972.

INITIAL DISTRIBUTION LIST

1. Defense Technical Information Center 2
    8725 John J. Kingman Rd., Suite 0944
    Ft. Belvoir, VA 22060-6218

2. Dudley Knox Library 2
    Naval Postgraduate School
    411 Dyer Rd.
    Monterey, CA 93943-5101

3. Dr. Wolfgang Send 1
    DLR – Institute of Aeroelasticity
    Bunsenstr. 10
    D-37073 Göttingen Germany

4. Prof. Max F. Platzer, Code AA/Pl 3
    Department of Aeronautics and Astronautics
    Naval Postgraduate School
    Monterey, CA 93943-5000

5. Dr. Kevin D. Jones, Code AA/Jo 3
    Department of Aeronautics and Astronautics
    Naval Postgraduate School
    Monterey, CA 93943-5000

6. Dr. Hebbar, Sheshagiri, Code AA 1
    Department of Aeronautics and Astronautics
    Naval Postgraduate School
    Monterey, CA 93943-5000

7. Lt Raymond O'Hare 1
    45773 Stoneu Run Dr.
    Great Mills, MD 20634

8. Lt Timothy C. Lund 2
    313 7th St.
    Pacific Grove, CA 93950